



**Utrecht University**

*Master Thesis*

**Beauty of the Quark Gluon Plasma**  
Prospect for  $B^0$  measurement in ALICE

Lennart van Doremalen  
Student number - 3377369  
Utrecht University

**Supervisor**  
Dr. André Mischke

**Daily Supervisor**  
Dr. Alessandro Grelli

February 1, 2017



### Abstract

We studied the feasibility of  $B^0$  meson measurement in ALICE to determine the properties of the Quark-Gluon Plasma, a form of matter in which quarks and gluons are deconfined. This plasma is expected to have existed in the early universe and in present-day neutron stars. We specifically studied the prospect of reconstructing the  $B^0$  with the full hadronic decay channel  $B^0 \rightarrow D^{*-} \pi^+ \rightarrow \overline{D^0} \pi^- \pi^+ \rightarrow \pi^- K^+ \pi^- \pi^+$ . We show that we can successfully reconstruct the  $B^0$  using this decay channel in Monte Carlo simulations and calculate expectations for the analysis in data.





**The road not taken**

Two roads diverged in a yellow wood,  
And sorry I could not travel both  
And be one traveler, long I stood  
And looked down one as far as I could  
To where it bent in the undergrowth;

Then took the other, as just as fair,  
And having perhaps the better claim,  
Because it was grassy and wanted wear;  
Though as for that the passing there  
Had worn them really about the same,

And both that morning equally lay  
In leaves no step had trodden black.  
Oh, I kept the first for another day!  
Yet knowing how way leads on to way,  
I doubted if I should ever come back.

I shall be telling this with a sigh  
Somewhere ages and ages hence:  
Two roads diverged in a wood, and I  
I took the one less traveled by,  
And that has made all the difference.

- *Robert Frost*

# Contents

|          |   |           |
|----------|---|-----------|
| <b>1</b> | <b>Introduction</b>   | <b>5</b>  |
| <b>2</b> | <b>Summary for non-physicists</b>   | <b>6</b>  |
| <b>3</b> | <b>Theoretical Background</b>   | <b>7</b>  |
| 3.1      | The Standard Model . . . . .  | 7         |
| 3.2      | Quantum Chromodynamics . . . . .  | 8         |
| 3.2.1    | Confinement . . . . .   | 8         |
| 3.2.2    | Asymptotic freedom . . . . .  | 8         |
| 3.3      | The Quark-Gluon Plasma . . . . .  | 9         |
| <b>4</b> | <b>Experimental Background</b>  | <b>11</b> |
| 4.1      | Colliders and QGP formation . . . . .   | 11        |
| 4.2      | Evolution of the QGP . . . . .  | 12        |
| 4.3      | Heavy quarks as probe of the QGP . . . . .  | 12        |
| 4.4      | Current Nuclear Modification Results for Heavy Quarks . . . . .                   | 14        |
| <b>5</b> | <b>A Large Ion Collider Experiment</b>  | <b>16</b> |
| 5.1      | Detectors . . . . .   | 17        |
| 5.1.1    | Inner Tracking System . . . . .   | 17        |
| 5.1.2    | Time Projection Chamber . . . . .   | 17        |
| 5.1.3    | Time of Flight detector . . . . .   | 18        |
| 5.1.4    | Electromagnetic Calorimeter . . . . .   | 19        |
| 5.2      | Detector upgrade . . . . .  | 19        |
| 5.3      | Data analysis framework . . . . .   | 21        |
| <b>6</b> | <b><math>B^0</math> - Production and Decay</b>                                    | <b>22</b> |
| 6.1      | Beauty Production and Fragmentation . . . . .                                     | 22        |
| 6.2      | Promising decay chains . . . . .  | 23        |
| 6.3      | Expected $B^0$ production for selected decay chain . . . . .                      | 25        |
| 6.3.1    | Number of $B^0$ mesons in pp collisions at $\sqrt{s} = 7$ TeV . . . . .           | 25        |
| 6.3.2    | Number of $B^0$ mesons in p-Pb collisions at $\sqrt{s_{NN}} = 5.02$ TeV . . . . . | 26        |
| <b>7</b> | <b><math>B^0</math> - Reconstruction and Candidate Selection</b>                  | <b>27</b> |
| 7.1      | Reconstruction . . . . .  | 27        |
| 7.1.1    | Quality assessment . . . . .  | 28        |
| 7.2      | Candidate selection . . . . .   | 31        |
| <b>8</b> | <b>Results</b>  | <b>33</b> |
| 8.1      | Data sets . . . . .   | 33        |
| 8.2      | Results for pp collisions at $\sqrt{s} = 7$ TeV . . . . .                         | 38        |
| 8.2.1    | Monte Carlo Simulation . . . . .  | 38        |
| 8.2.2    | Expectation in Data . . . . .   | 41        |
| 8.2.3    | Data . . . . .  | 43        |
| 8.2.4    | Minimum Bias . . . . .  | 43        |

|           |   |           |
|-----------|---|-----------|
| 8.3       | Results for p-Pb collisions at $\sqrt{s_{NN}} = 5.02$ TeV . . . . . | 43        |
| 8.3.1     | Monte Carlo Simulation . . . . .                                    | 43        |
| 8.3.2     | Expectation in Data . . . . .                                       | 46        |
| 8.3.3     | Data . . . . .  | 48        |
| 8.4       | EMCal trigger exploration . . . . .                                 | 48        |
| <b>9</b>  | <b>Discussion and Conclusions</b>                                   | <b>49</b> |
| <b>10</b> | <b>Acknowledgment</b>   | <b>50</b> |

# Chapter 1

## Introduction

The study of the universe at a fundamental level has resulted in an extensive model which can successfully describe all known subatomic particles and their interactions through the Electromagnetic, Weak, and Strong force. In this Standard Model of particle physics, the strong force is described by the theory of Quantum Chromodynamics (QCD). QCD predicts the existence of a state of matter in which quarks and gluons are deconfined, a quark-gluon plasma (QGP). The phase transition of hadrons to a QGP is only expected to occur in systems with a very high energy density. In nature, this energy density is only expected to be found in the extreme temperatures directly after the Big Bang and in ultra dense neutron stars. So, in order to test and expand our understanding of the strong force we can study the behavior of matter in these extreme conditions. One way to do this is by recreating the characteristics of the early universe with heavy-ion collisions using particle accelerators.

The Large Hadron Collider at CERN is the biggest particle collider to date and is home to the heavy-ion physics dedicated experiment called ALICE. In order to study the properties of the QGP, the experiment measures collision data of lead ions, protons, and a combination of the two. Collisions of protons, in which no QGP formation is expected, are used as reference to distinguish the effects that are caused by the QGP formation in other events. This results in key observables like the nuclear modification factor and the anisotropic flow of the QGP. Heavy quarks (charm and beauty) are created earlier in the collision, allowing them to experience the full evolution of the hot and dense matter formed by the colliding particles. The beauty quark and its fragmentation products are therefore an interesting candidate for future heavy-ion physics in ALICE.

In this thesis, we studied the prospect of using fully hadronically reconstructed  $B^0$  mesons originating from the QGP to study the properties of this phase of matter. First, we will briefly explore the theoretical background of Quantum Chromodynamics, the Standard Model, and the quark-gluon plasma in chapter 3. Second, we will look at the experimental background of QGP research in chapter 4. Third, we will give an overview of ALICE and the used detectors in chapter 5. In chapter 6, we study the production and decay of the  $B^0$  meson. In chapter 7, we study the reconstruction and selection of the  $B^0$  meson candidates. The results of the analysis is presented in chapter 8. Finally, we conclude this thesis with the discussion and conclusion in chapter 9. A summary for non-physicists is given directly after the introduction in chapter 2.

## Chapter 2

# Summary for non-physicists

All of the things we see in our daily live are made of atoms, extremely small particles that can only be seen with the strongest microscopes. In ancient Greece, philosophers had hypothesized that nature is made up of indivisible objects, which they called atoms (coming from the Greek word for uncuttable). When scientist in the 19th century found particles they could not divide further they called these particles atoms.

Today, we know that atoms are not indivisible. They consist of a core called the nucleus and an electron cloud that both carry an electric charge that keeps the two together. The nucleus is made up of even smaller particles called neutrons and protons. And even these particles can be divided further in particles we call quarks and gluons.

As far as we understand now these quarks and gluons are, along with electrons, the fundamental particles that make up the universe. A significant part of this was discovered using particle collider experiments. In these experiments, we accelerate particles in a machine and smash them against each other or something else. Then, we use detectors to detect what happened during and after the collision. Also other machines were used but we won't go into too much detail here.

The data from particle collider experiments has resulted in a detailed understanding of the fundamental laws of the universe. We know now that the quarks and gluons that make up the protons and neutrons are being held together in these bound states by a force we call the strong force. This force is so strong and peculiar that quarks and gluons can never be free from one another except in the most extreme circumstances.

The only places in nature that are extreme enough are the first microseconds after the Big Bang (the moment in which the universe was formed) and the supremely massive Neutron stars.

Using particle colliders we can recreate the conditions after the Big Bang by colliding atoms, which have been accelerated to a speed near the speed of light (light travels at a speed of 299.792.458 meter per second). This allows us to study the properties of the free quarks and gluons. We call the state of matter created by the collision a Quark-Gluon Plasma (QGP).

We cannot measure the properties of the Quark-Gluon Plasma directly, rather we need to detect particles which originate from the collision and use these to determine the properties of the Quark-Gluon Plasma. This is currently being done at the ALICE experiment at the Large Hadron Collider at CERN.

For this thesis, we study the feasibility of using a specific particle to study the Quark-Gluon Plasma. We have made a computer code that uses the data collected by ALICE to find the particle that we are interested in. The code is successful during simulations and could be successful with real data, but we will need more data to have a chance to find it. If the code is eventually successful in data we gain information, which can be used to increase our understanding of the early universe and the working of the strong force that keeps the quarks and gluons together.

## Chapter 3

# Theoretical Background

### 3.1 The Standard Model

The Standard Model is the most successful model to date in describing the known particles and their interactions. The model is however also recognized to be incomplete since it does not include phenomena like dark energy, dark matter, and gravity. The Standard Model is a quantum field theory in which the particles and their interactions are mathematically formulated as a Lagrangian that is invariant under the gauge transformations of the symmetry groups:

$$SU(3)_C \times SU(2)_L \times U(1)_Y$$

where C, L, and Y stand for color, left-handedness, and weak hypercharge respectively. The Lagrangian includes terms for all known particles, Electromagnetism, the weak force, the strong force, and the Higgs mechanism. Interactions between particles are mediated by bosons. Figure 3.1 shows the particles of the Standard Model. These particles can decay in other particles under the condition that conserved quantities like energy, charge, and momentum are preserved.

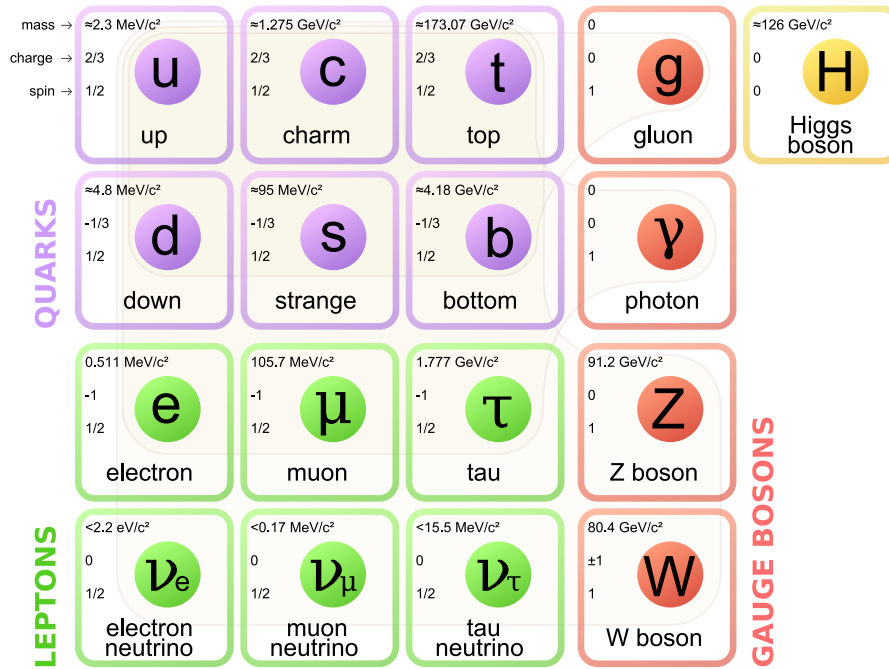


Figure 3.1: Elementary particles in the Standard Model.[1]

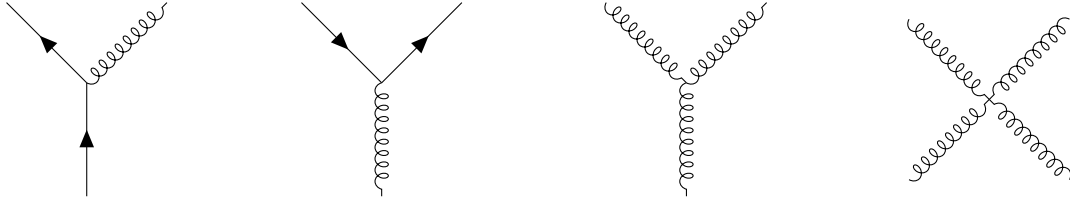


Figure 3.2: First order QCD interactions. From left to right the images show gluon radiation, gluon splitting, and gluon self-coupling. Adapted from [7].

## 3.2 Quantum Chromodynamics

Quantum Chromodynamics (QCD) is the theory that describes the interactions by the strong force, which are illustrated in figure 3.2. This force is mediated by gluons and couples to all particles with a color charge. Both quarks and gluons possess this charge, which results in the formation of hadrons. The most common hadrons are neutrons and protons, which are the building blocks of atomic nuclei. In high energy physics also other hadrons are formed. These hadrons are grouped into categories like baryons, consisting of three (anti-)quarks, and mesons, consisting of a quark and an antiquark. Most hadrons only have a very short lifetime, which means that only a handful of these particles can be detected directly in particle detectors like those at the Large Hadron Collider. An important property of QCD is that quarks always appear in a bound hadron state, so we cannot detect individual quarks. This aspect of QCD is called confinement and only in a QGP can quarks move unbound due to an effect called asymptotic freedom. We will study both phenomena more closely in the next sections.

### 3.2.1 Confinement

Experimentally, quarks have never been seen to exist in a free isolated state, only in bound color neutral states. As of yet, there is no analytical proof that explains this phenomenon but the main theory is that the confinement arises due to the effect of gluon self-interaction on the potential between two quarks. This potential is approximated as a Coulomb potential plus a linear potential:

$$V_{q\bar{q}}(\vec{r}) = -\frac{4\alpha_S(Q^2)}{3r} + \kappa r,$$

where  $\alpha_S$  is the strong coupling constant,  $r$  is the absolute distance between the quarks, and  $\kappa$  is a string tension constant. The linear string tension component arises due to a self-interacting gluon string that appears between the two separated quarks. Once the string reaches a certain size, it becomes energetically more favorable to create a new quark-antiquark pair than to increase the string length. This effectively prevents quarks from appearing free in nature.

### 3.2.2 Asymptotic freedom

The coupling constant used in the previous equation is, despite its name, not constant but a variable that depends on the momentum transfer between the interacting quarks. When quarks exchange more momentum the strength of their coupling decreases. To first-order approximation the coupling strength is defined as:

$$\alpha_S(Q^2) = \frac{12\pi}{(11N_c - 2N_f) \cdot \ln(Q^2/\Lambda_{QCD}^2)},$$

where  $N_c = 3$  is the number of colors,  $N_f$  is the number of quark flavors with a mass below the used renormalization scale, and  $\Lambda_{QCD} \approx 200$  MeV is a scale parameter that also depends on the renormalization scale. This scale parameter also indicates the regime where the strong coupling constant becomes too large for reliable perturbative QCD calculations. In high energy physics, where the constant is expected to be small, this means that experimental measurements can be used to test the predictions of perturbative QCD. The asymptotic behaviour of the strong force is visible in both theoretical QCD predictions and experimental measurements of the strong coupling constant. This is shown in figure 3.3.

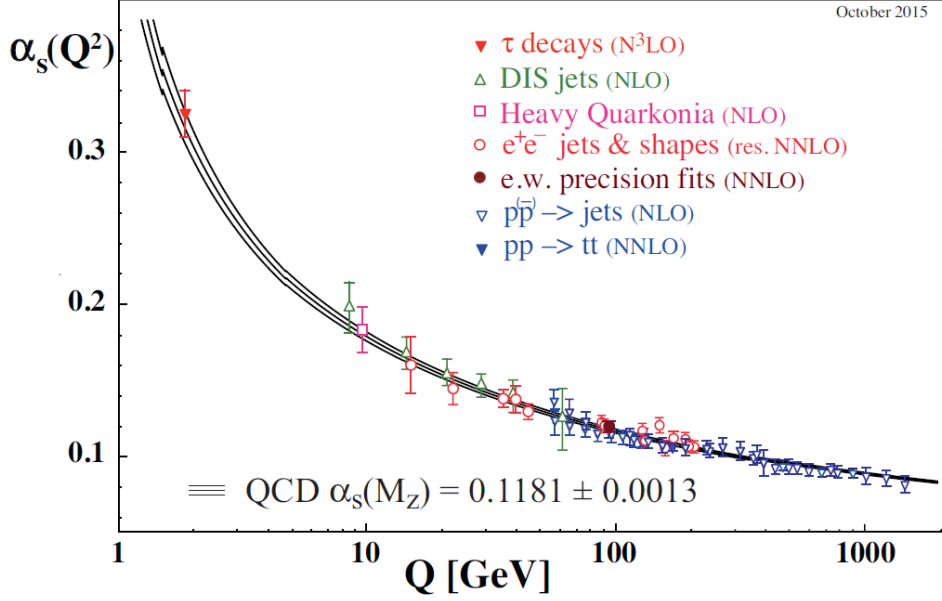


Figure 3.3: Measurements and theoretical prediction of the QCD coupling constant as a function of the four-momentum transfer.[3]

### 3.3 The Quark-Gluon Plasma

At extremely high temperatures and/or densities the asymptotic freedom is expected to result in a state of hot and dense matter in which quarks and gluons are deconfined. These free particles form a Quark-Gluon Plasma. In this plasma, the color charges of the quarks and gluons is screened while the QGP as a whole remains color neutral.

In figure 3.4, the QCD phase diagram is shown. The diagram shows the QCD phases as a function of temperature and baryo-chemical potential. The baryo-chemical potential is the excess of matter over anti-matter. This potential scales with the (baryon) density of the system, so ultra-dense objects like neutron stars could be dense enough to have an interior made of a QGP at a relatively low temperature. Systems with a low baryon chemical potential are expected to have a continuous phase transition, with a transition temperature around  $T \approx 170$  MeV ( $2 \times 10^{12}$  Kelvin).

The universe is expected to have been formed by a Big Bang followed by a rapid period of inflation. During the first microseconds of the Big Bang the universe was hot and dense enough to be completely filled with a quark-gluon plasma. The main school of thought is that the universe began with equal amounts of matter and anti-matter, although there is no explanation at this time why this balance is not seen in the present day universe. Assuming this hypothesis is correct, the early universe will have had a net zero baryo-chemical potential. That means that the evolution of the early universe should occur in the same region of the phase diagram as the experimental reach of the LHC.

The interactions that happen inside the QGP produced at the LHC are dominated by strong interactions. This is because the strength and timescale at which particle interactions occur depend on the coupling constant of the mediating force. At low energies the strong force has a coupling constant of  $\alpha_s = 1$ , the electromagnetic force  $\alpha_e = 1/137$ , and the weak force  $\alpha_w = 10^{-6}$ . The coupling constants of the strong and weak force do become smaller at higher energies while the coupling constant for the electromagnetic force becomes larger, but the strong force remains dominant within the energy reach of the LHC.



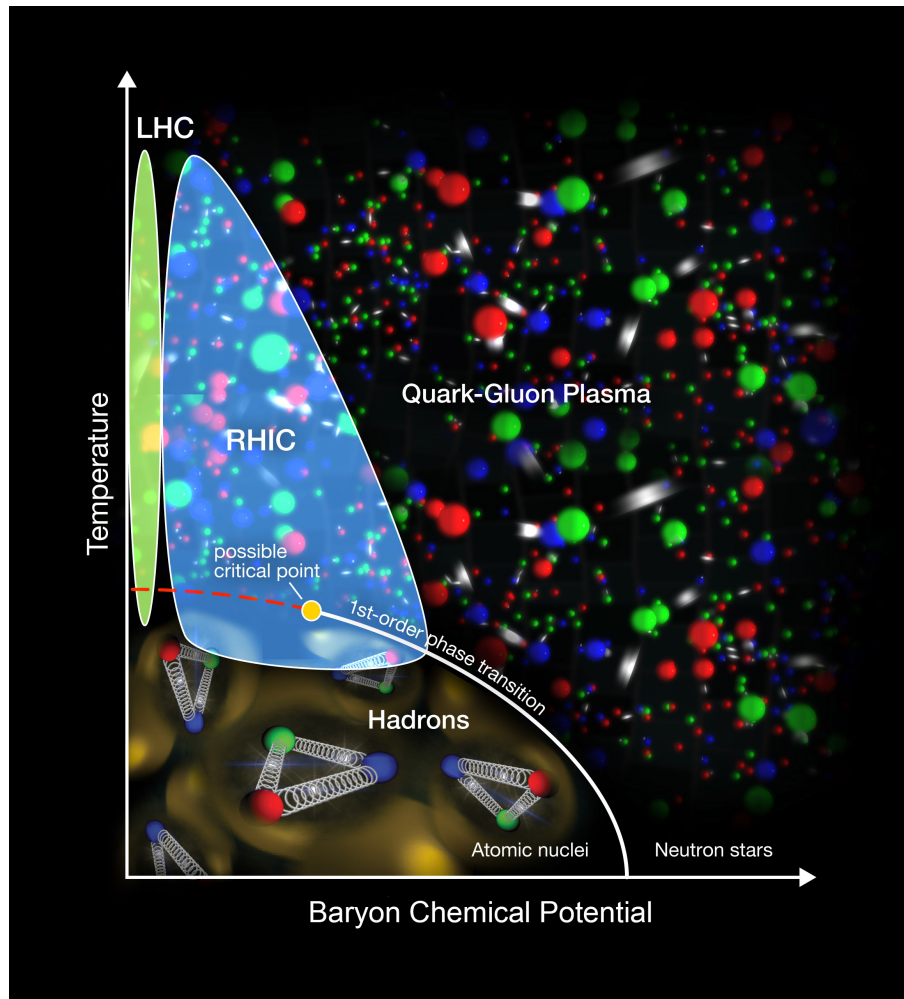


Figure 3.4: QCD phase diagram showing the reach of current particle accelerators. Adapted from [19].

## Chapter 4

# Experimental Background

### 4.1 Colliders and QGP formation

In order to study the QGP, we first have to create one. This can be achieved by using particle colliders to collide heavy nuclei at ultra-relativistic energies. The LHC is one of those colliders. It is a large synchrotron particle accelerator, which has a circular design with a circumference of 27 kilometers.

The collider works by using magnets to bend and focus the charged particles as they go through the ring of the accelerator. The particles experience a Lorentz force ( $F = q\vec{v} \times \vec{B}$ ) due to the magnetic fields generated by the magnets. The strength of the magnetic fields is increased as the energy of the beam is raised to the desired level. This increases the bending strength of the magnets, thus making sure that the beams stay within the beam pipes.

The particles in the beam are accelerated to higher energies by radio-frequency cavities. These cavities are made with a specific size and shape so that an electromagnetic field of 400 MHz becomes resonant inside the cavity. Charged particles are accelerated by the field during each pass until they have the desired velocity. The particles are also bunched by the field, particles that arrive exactly on time experience no acceleration while particles that go too fast/slow are decelerated/accelerated with respect to the other particles. This is illustrated in figure 4.1.

Protons can be accelerated to an energy of 7 TeV in the LHC. Lead ions have a larger positive charge than a proton (82 times to be exact) but they also have a higher mass per charge ratio. So the total energy ( $82 \times 7$  TeV) is divided over the 208 nucleons of the used lead isotope, this gives an energy of 2.76 TeV per nucleon for Pb-Pb collisions.

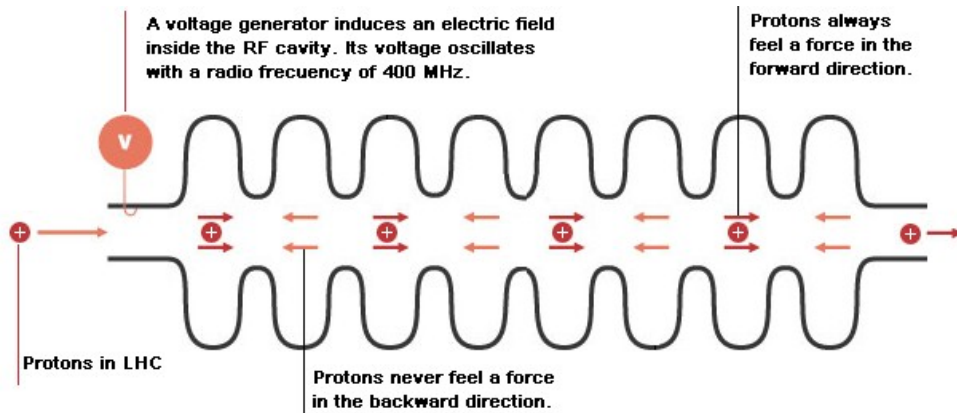


Figure 4.1: Illustration of a radio-frequency cavity in the LHC.[15]

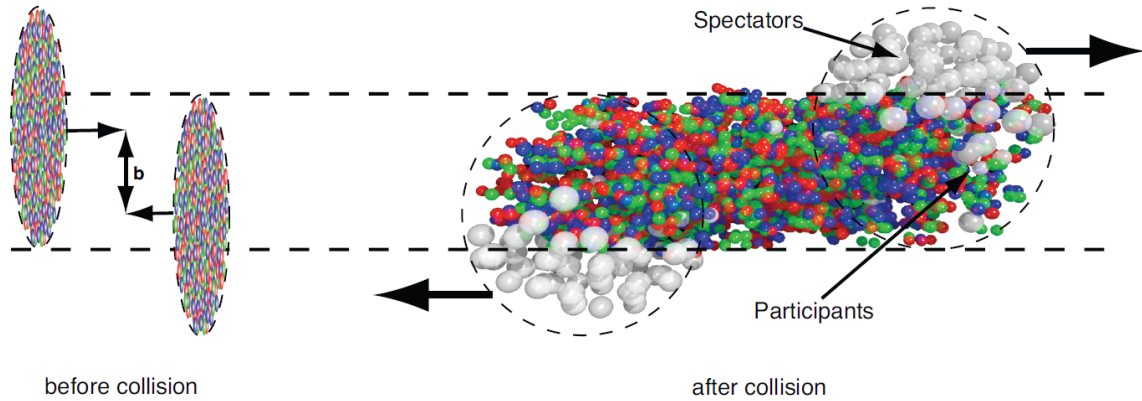


Figure 4.2: A depiction of the system before and after of two colliding heavy ions. The nuclei collide with an impact parameter  $b$ , which limits the number of nucleons that participate in the collision.[7]

The particles are subsequently collided in the different experiments along the beam. Not all particles hit each other, and those particles that do hit each other collide with a certain impact parameter. The collision result in a mass of hot and dense matter that can form a QGP if its energy density is high enough.

## 4.2 Evolution of the QGP

The collision and the space-time evolution of the QGP is described in the Bjorken model. The two relativistic nuclei, which can be seen as flat discs due to Lorentz contraction, pass through each other and leave a group of highly excited particles behind in the interaction region. This is shown in figure 4.2 and as the pre-equilibrium phase ( $t < \tau_0$ ) in figure 4.3. The production of the excited particles happens in a time scale of the order of 0.1 fm/c. The particles interact with each other and de-excite into new quarks and gluons. A mass of hot and dense matter is formed that quickly thermalizes in a time of approximately 1 fm/c. At this time ( $t = \tau_0$ ) the quark-gluon plasma is formed.

The QGP behaves like a near perfect liquid with almost no viscosity.[1] The temperature creates a thermal pressure, which causes the QGP to expand. This expansion cools the QGP until it reaches the phase transition temperature of  $T_C \approx 170$  MeV. At this point the QGP has lived for approximately 10 fm/c and will start to hadronize. When the mass reaches the chemical freeze out temperature  $T_{Ch}$ , the QGP has completely hadronized into a hadron gas and the hadrons no longer undergo chemical transitions (i.e. they are fixed from changing to another type of hadron except through decay).

The hadrons in the hadron gas continue to interact with each other while the gas expands. This keeps the hadrons in a kinetic equilibrium. When the gas reaches the kinetic freeze out temperature  $T_{fo}$  the particle interactions no longer maintain equilibrium. The particles move away from the collision point and will have a chance to decay depending on their lifetime. The detectors will then measure those particles or their decay products when they interact with the detectors.

## 4.3 Heavy quarks as probe of the QGP

By measuring the particles that originate from the QGP we can study the properties of the QGP. The sensitivity of these particles to key QGP observables depends on the time at which the particle is created and its subsequent interactions with the QGP. Heavy quarks are of particular interest due to their early formation time. The formation time can be estimated from the quark pair production Feynman diagram and is inversely proportional to the mass of the quark:

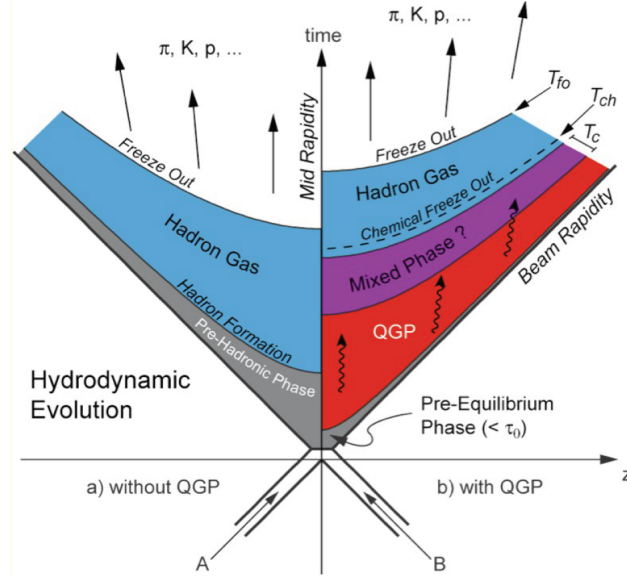


Figure 4.3: Space-time evolution of a heavy-ion collision without (left) and with QGP formation (right).[1]

$$\tau_q \approx \frac{\lambda_{compton}}{c} = \frac{\hbar}{2m_q c^2}.$$

This means that heavier quarks are produced earlier in the collision. The beauty quark is expected to be produced before the formation of the QGP and should therefore be able to experience the full space-time evolution of the QGP.

Particles that are produced in a collision can be subject to initial and final state effects:

- **Initial state effects** - are effects that affect the hard cross section of the collision. These effects are caused by the properties of the collision. They include the size of the colliding particles and energy at which they collide.
- **Final state effects** - are caused by the generated medium. These effects can influence the yields and the kinematic properties of the produced particles in a way that depends on the properties of the medium.

Collisions in which no QGP is created serve as a benchmark for collisions in which a QGP is created. In the collisions without a QGP only the initial state effects are present. When we study collisions with a QGP we observe both initial and final state effects. Using the benchmark collisions we can disentangle both contributions which allows us to study the final state effects due to the medium.

The final state effects with respect to the benchmark are given by the nuclear modification factor:

$$R_{AA}(p_T) = \frac{1}{\langle N_{coll} \rangle} \frac{dN_{AA}/dp_T}{dN_{pp}/dp_T},$$

where the number of detected particles in a specific  $p_T$  range  $N_{AA}$  for a heavy-ion collision are compared with the same number in a proton-proton collision. The detected number of particles for the pp collision is scaled by a constant  $\langle N_{coll} \rangle$ . This constant is based on the number of binary collisions that are expected in a nucleus-nucleus collision. We assume that heavy-ion collisions can be approximated as a superposition of pp collisions. So, if there are no nuclear or QGP effects the nuclear modification factor will be equal to one.

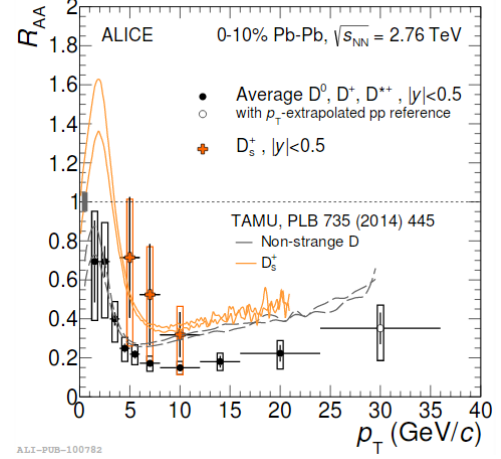
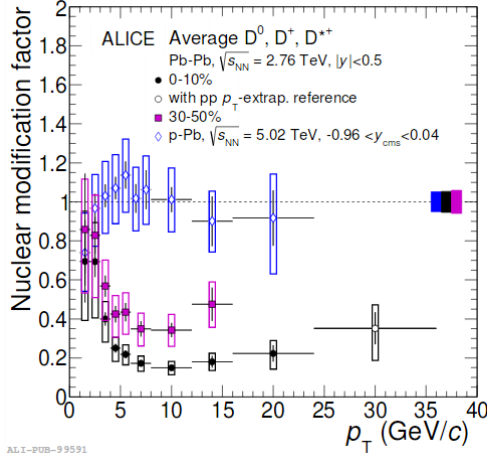


Figure 4.4: Left: The nuclear modification factor for charmed mesons for different collision types as a function of  $p_T$ . Right: Nuclear modification factor results for D mesons as a function of  $p_T$  for Pb-Pb collisions and corresponding theoretical predictions.[18]

The quarks that move through the QGP lose energy by interaction with the quarks and gluons in the QGP, and by the radiation of gluons while passing through the medium. This radiation is suppressed by the dead-cone effect for heavier quarks:

$$\theta_{\text{dead-cone}} < \frac{m_q}{E_q}.$$

This leads to a smaller suppression of the Nuclear Modification factor for the beauty quark compared to lighter quarks. The beauty quark is therefore a very interesting probe of the QGP.

## 4.4 Current Nuclear Modification Results for Heavy Quarks

ALICE has been successful in measuring the nuclear modification factor for charmed mesons. Some of these results are shown in figure 4.4. The measurement of beauty mesons will be a next step for ALICE. No nuclear modification factor measurements for these mesons have been published by ALICE to this date.

The CMS experiment does have measurements of the nuclear modification factor for beauty mesons. These results are shown in figure 4.5 and 4.6. One of the challenges for ALICE will be to improve on these results.

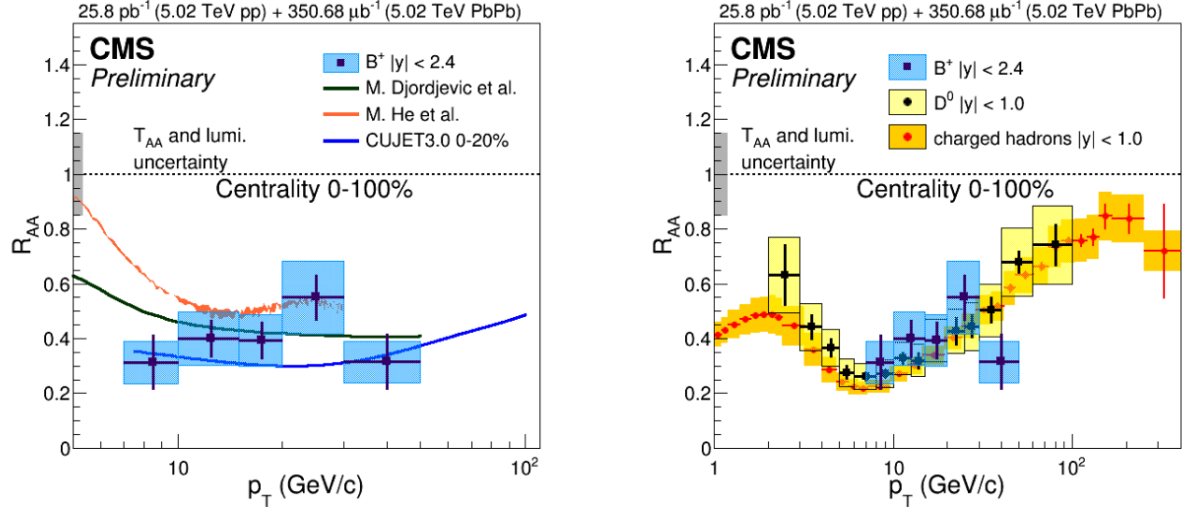


Figure 4.5: The Nuclear Modification Factor for the  $B^+$  in Pb-Pb collisions, as measured by CMS. (left) Including theoretical predictions. (right) Including the Nuclear Modification Factor measurements for other particles.[16]

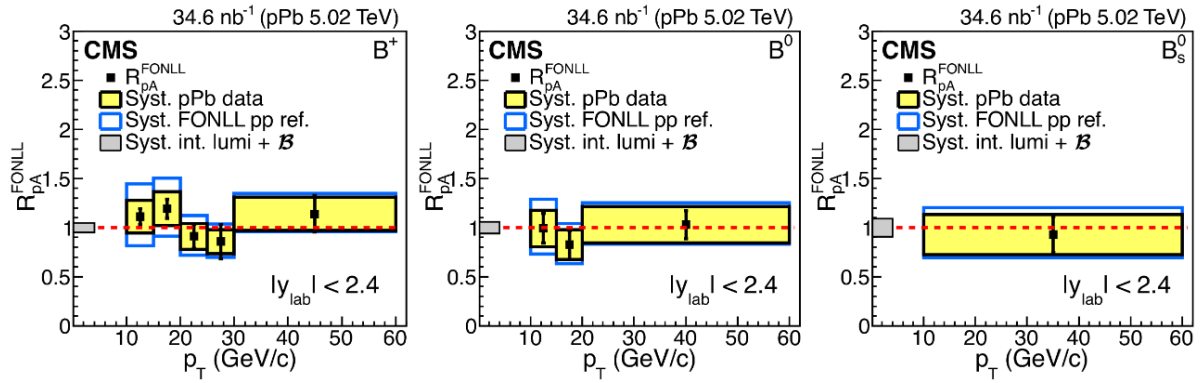


Figure 4.6: The CMS results for the Nuclear Modification Factor in p-Pb for different beauty mesons as a function of  $p_T$ . [17]



## Chapter 5

# A Large Ion Collider Experiment

ALICE is the acronym for "A Large Ion Collider Experiment" and it is one of the major experiments that is being performed at the Large Hadron Collider. The experiment has been designed for the analysis of heavy ion collisions. Its goal is to study the strongly interacting matter that is created in these collisions.

The detector itself is 26 meter long, 16 meter high, and 16 meter wide. Figure 5.1 shows an overview of the experiment. It consists of a large number of specialized detectors and is placed at a distance of 56 meter beneath the ground. The detectors collect specific data from the produced particles that allows us to study the collision events.

In this chapter we will discuss a number of the detectors that were most important for this thesis and describe their role in the reconstruction process. We will also discuss the upcoming upgrade of ALICE and the framework used for analyses.

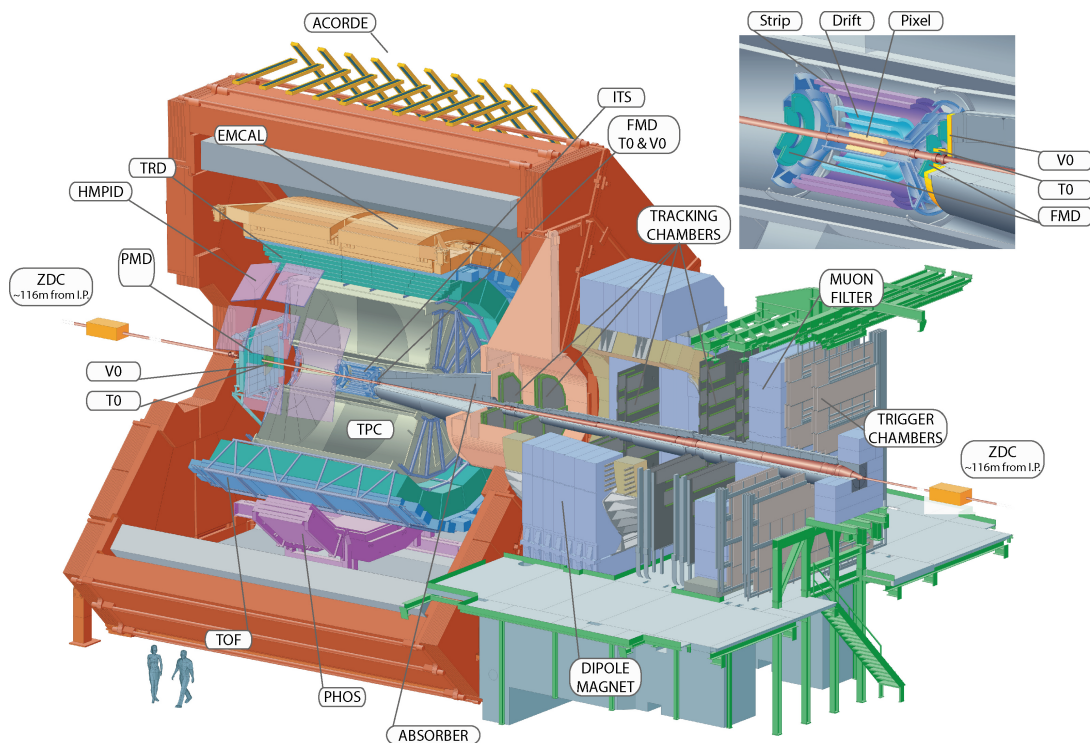


Figure 5.1: A schematic overview of ALICE and its detectors.[1]

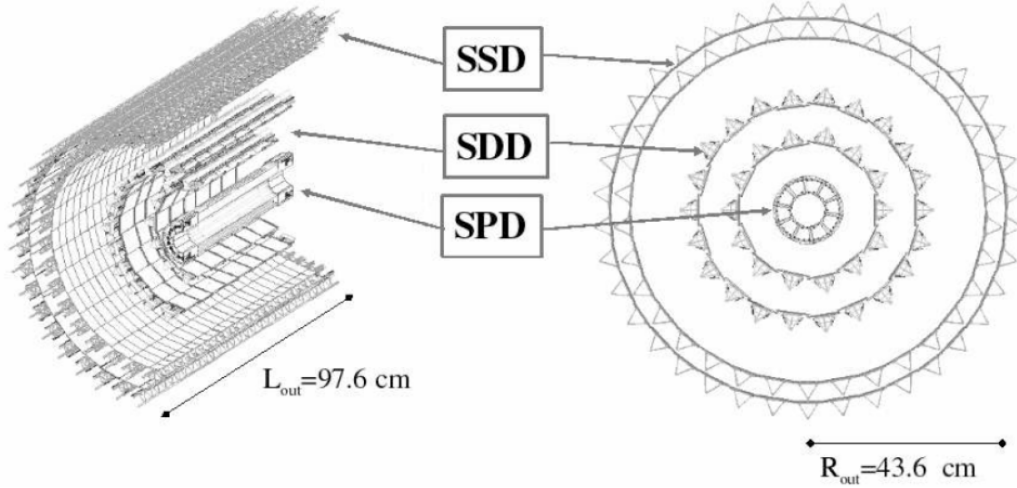


Figure 5.2: A schematic overview of the Inner Tracking System and the different detector layers that make up the ITS.[5]

## 5.1 Detectors

### 5.1.1 Inner Tracking System

The Inner Tracking System (ITS) is the detector that is closest to the primary collision point. The purpose of the detector is to determine the vertex positions of the primary vertex and secondary decay vertices with a high precision. It is also designed to identify and track low momentum particles. The detector also improves the momentum resolution of reconstructed tracks when combined with the TPC.

- **SPD** - The first two layers consists of Silicon Pixel Detectors (SPD). They are positioned at a distance of 3.9 cm and 7.6 cm from the beam axis respectively. Their resolution in the  $r\phi$ -plane is with  $12\ \mu\text{m}$  the largest of all layers. In the  $z$  direction the SPD has a precision of  $100\ \mu\text{m}$ .
- **SDD** - The second pair of layers are made of Silicon Drift Detectors (SDD). These layers are placed at a distance of 15 cm and 23.9 cm from the beam axis. They have a resolution of  $38\ \mu\text{m}$  in the  $\phi$ -plane and  $28\ \mu\text{m}$  in the  $z$  direction.
- **SSD** - The last pair of layers consists of Silicon Strip Detectors (SSD). Their distances to the beam axis are 38 cm and 43 cm. The  $r\phi$ -plane resolution of these detectors is  $20\ \mu\text{m}$ . In the  $z$  direction the resolution is limited to  $830\ \mu\text{m}$ .

The ITS detectors cover the full azimuthal range of the experiment. The pseudorapidity range of the SPD is with  $|\eta| < 1.95$  larger than the other detectors that have a range of  $|\eta| < 0.9$ .

### 5.1.2 Time Projection Chamber

The Time Projection Chamber (TPC) is the largest detector of ALICE. It supplies the majority of the tracking information for the detected particles. The TPC is a gas based detector, charged particles that traverse the detector will ionize the gas and thereby free electrons. A electric field with a strength of  $400\ \text{V/cm}$  is applied over the length of the detector. The freed electrons are accelerated by this field towards the end caps of the TPC. At these end caps there are Multi-Wire Proportional Chambers (MWPCs) to detect the ionization signal. While the electrons move trough the gas at the MWPCs the electrons ionize additional atoms which results in an ionization cascade that gives an amplified signal.

The TPC detects the specific ionization energy loss  $dE/dx$  of the particles that pass through the detector. This energy loss depends on the type of particle that interacts with the gas. The energy loss also



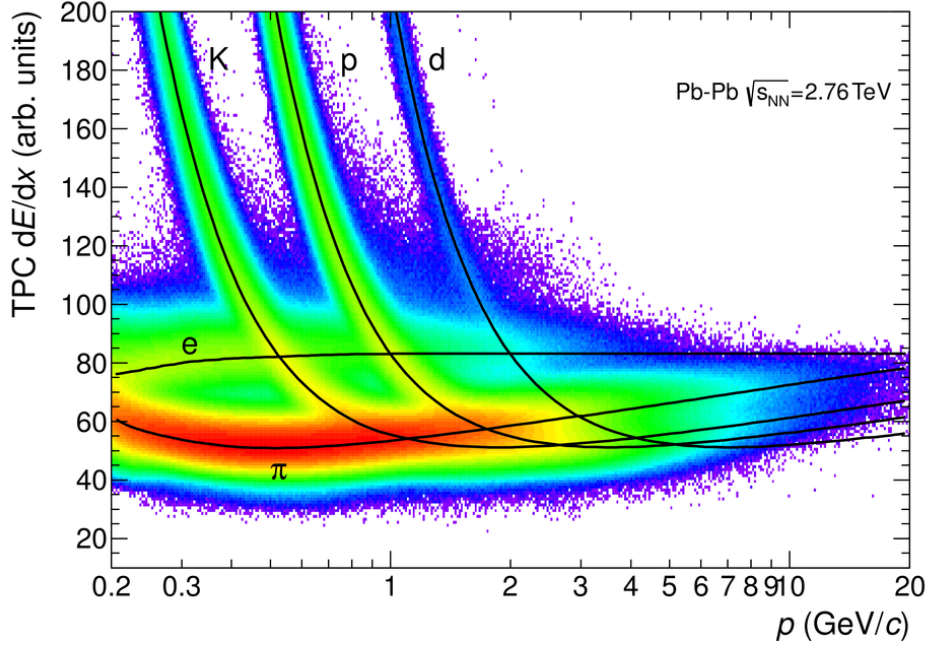


Figure 5.3: Diagram showing the specific ionization energy loss of different particles in the TPC. The black lines show the Bethe-Bloch parametrization.[2]

depends on the momentum of the particle and can be described with the Bethe-Bloch equation. Figure 5.3 shows the specific ionization energy loss for particles detected in the TPC. As can be seen in this plot the energy loss regions of several particles overlap. This means that the particle identification capability of the TPC works best in the low momentum region in which there is less overlap.

The TPC is also important for the momentum determination of the detected particles. Timing information from other detectors is used to determine the drift duration of the electrons. This gives the z-position of the track, while the arc of the ionization track shows the movement of the track in the xy-plane under the influence of the magnetic field. The combination of the track curvature information of the TPC and the ITS along with information from other detectors gives the final momentum hypothesis of the particle track.

The TPC extends around the entire beam pipe and has a length of 5 meter. It starts at a radius of 85 cm and ends at a radius of 247 cm. It has a pseudorapidity coverage of  $|\eta| < 0.9$ , and a coverage up to  $|\eta| < 1.5$  with decreased momentum resolution.

### 5.1.3 Time of Flight detector

The Time of Flight detector (TOF) is a Multi-gap Resistive-Plate Chamber detector (MRPC). It is made of glass plates with gas between the plates. A voltage difference is applied on the beginning and end of each stack of plates which allows for the creation ionization avalanches in the gas by charged particles that pass through the detector. The glass plates stop the avalanches from passing to the next gas chamber, while readout electronics measure the signal produced between the plates.

The detector has a pseudorapidity coverage of  $|\eta| < 0.9$ . It extends from a radius of 370 cm to 399 cm and envelops the full azimuthal range of the experiment.

The arrival time of particles that go through the TOF detector can be measured with a precision of approximately  $\sim 80$  ps. This is an important part for the particle identification of particles with a momentum up to 2.5 GeV/c for pions and kaons. Using information from other detectors that measure

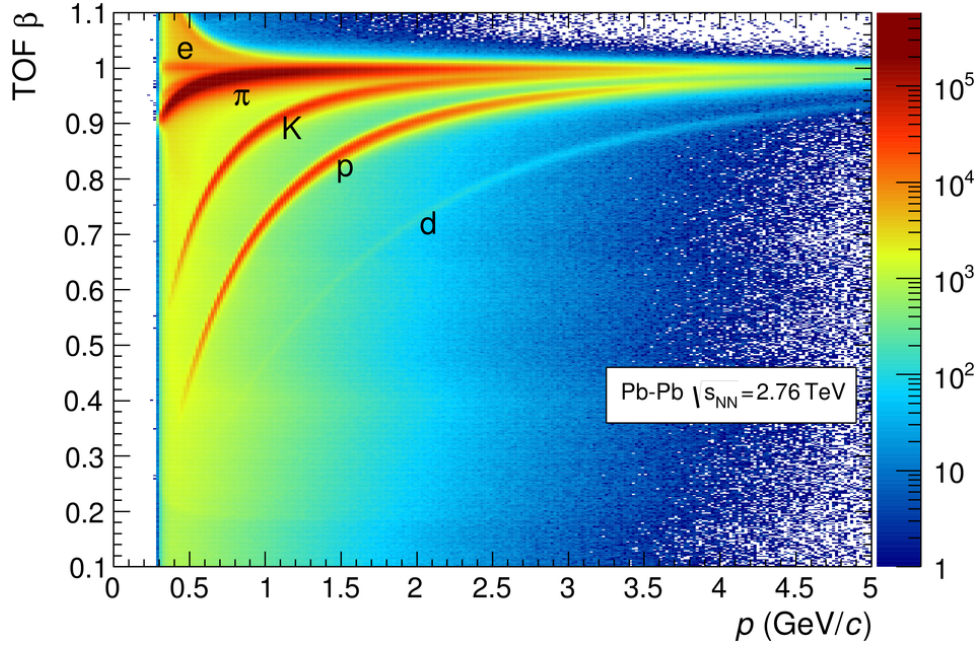


Figure 5.4: The time of flight for several particle species as a function of momentum measured by the TOF detector.[2]

the collision time, the TOF can determine the flight time of a particle. This gives the speed of the particle, which can be used along with the momentum hypothesis to give an estimate of the mass of the particle. The TOF is less effective at lower momenta, so the combination with the TPC gives the most accurate particle identification data. Figure 5.4 shows as an example the TOF measurement from Pb-Pb collisions.

#### 5.1.4 Electromagnetic Calorimeter

The Electromagnetic Calorimeter (EMCal) measures the energy deposition of particles that pass the detector, this deposition is proportional to the energy of the particle. Using the momentum information of the track supplied by the other detectors we can calculate the energy momentum ratio  $E/p$ . The energy deposition of a particle is mass dependent. Electrons will deposit almost all their energy while heavier particles will deposit less of their energy. Electrons can be identified by selecting the particles that have an energy momentum ratio close to one. A sketch of the EMCal is shown in figure 5.5.

The EMCal covers a smaller area than the other detectors we discussed. It has an acceptance of  $|\eta| < 0.7$  and  $80 < \phi < 187$ . We do not use this detector in this analysis due to its limited acceptance but it is worth mentioning because the EMCal can be used as a trigger. With this trigger events can be selected on specific properties. The beauty quark is produced in pairs and a significant percentage of these quarks decay semi leptonically. By triggering on these leptons it might be possible to get a higher number of beauty quarks per event.

## 5.2 Detector upgrade

ALICE is scheduled for an upgrade during the second long shutdown of the LHC. An important improvement will be the installation of a new Inner Tracking system. The new ITS will be placed closer to the collision point and will have a higher resolution, allowing for better vertexing and tracking of particles.

The new ITS will have seven layers compared to the current six. The Inner barrel will get an extra layer, with the first layer being placed at a radius of 22.4 mm. The new ITS is illustrated in figure 5.6 and a comparison of the upgraded ITS with the current ITS is shown in figure 5.7.

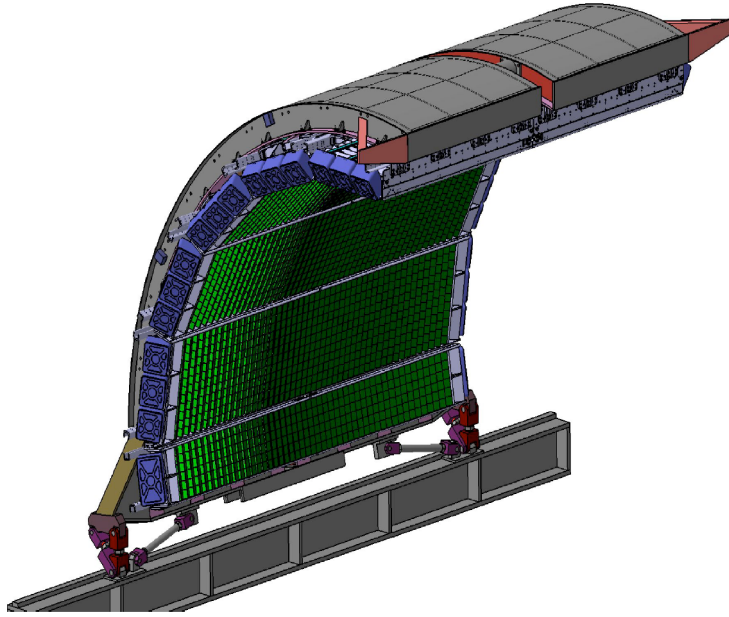


Figure 5.5: A graphical representation of the EMCal detector.[4]

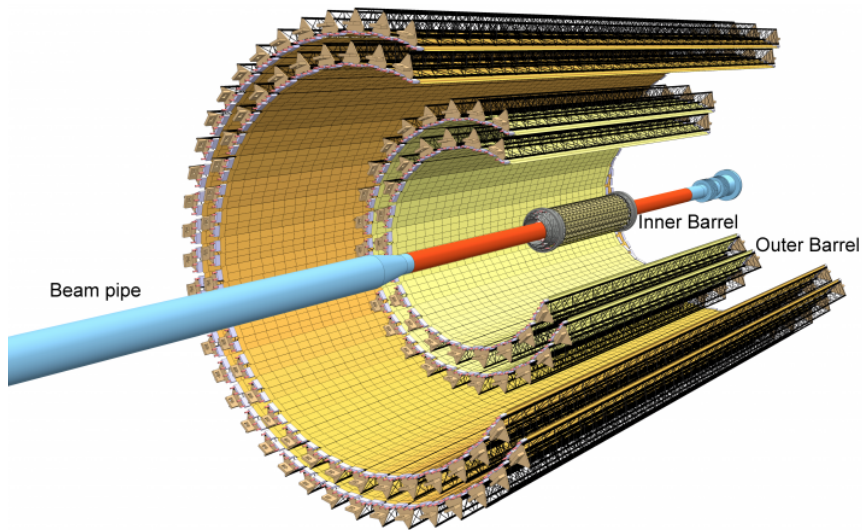


Figure 5.6: An illustration of the new Inner Tracking System, which will be installed during the second long shutdown of the LHC.[2]

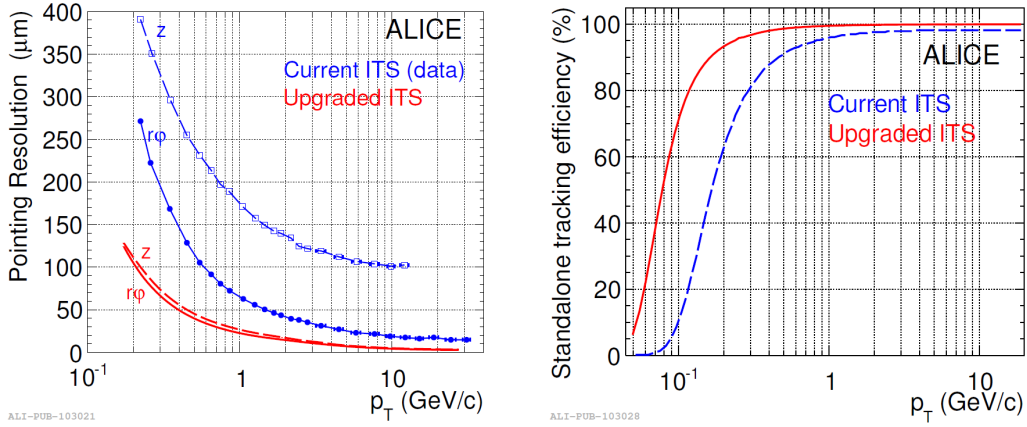


Figure 5.7: Graphs showing the improved resolution (left) and tracking efficiency (right) of the upgraded ITS compared to the current ITS.[10]

### 5.3 Data analysis framework

ALICE has its own analysis framework called AliRoot. This framework is an extended version of ROOT, which is the basis of many analysis programs being used throughout particle physics. ROOT, and AliRoot, are written in C++, an object-oriented programming language. The framework handles both simulation (Monte-Carlo) data and real data. It contains specific ALICE C++ classes that have to be used to access and analyze the collected/generated data.

Collision events are stored on the servers of the LHC. This data is used to reconstruct the particle tracks. After the reconstruction all data is saved as Event Summary Data (ESD) data files. These files are too big for general analysis tasks so the relevant data is saved in Analysis Object Data (AOD) data files. For the analysis in this thesis we use the AOD data files.

The analyses are performed on a large global computer network called the Worldwide LHC Computing Grid. Using this computing grid the time of performing an analysis can be reduced from months/years to hours/days.

## Chapter 6

# $B^0$ - Production and Decay

For this thesis, we want to study the feasibility of using fully hadronically reconstructed  $B^0$  mesons to study the QGP. In order to do this we need to study how many  $B^0$  mesons are produced in collisions at the LHC. First, we will look at the production of b-quarks (beauty) and the fragmentation of a beauty quark in a  $B^0$  meson, then we will explore the decay channels of the  $B^0$  and motivate the choice for the chosen decay channel. Finally, we will give an estimate of the number of  $B^0$  mesons we expect to be produced for the used decay channel.

We will also need to study our reconstruction performance and our ability to distinguish the  $B^0$  mesons from background noise. That will be the topic of chapter 8.

### 6.1 Beauty Production and Fragmentation

Beauty quarks are primarily created in  $b\bar{b}$ -pairs by pair creation, flavor excitation, and gluon splitting. Since the beauty quarks are heavy higher order contributions become small and their production can be calculated. We shall use literature values for the beauty quark production cross section in our calculations.

Once the beauty quark is produced it will form a bound state with another quark. The fragmentation of the beauty quark into hadrons has been measured by the DELPHI Collaboration in  $e^+e^-$  collisions.[1] The result is shown in figure 6.1. In this figure, it can be seen that the fragmentation of the beauty quark into a  $B^0$  meson is approximately 41%.

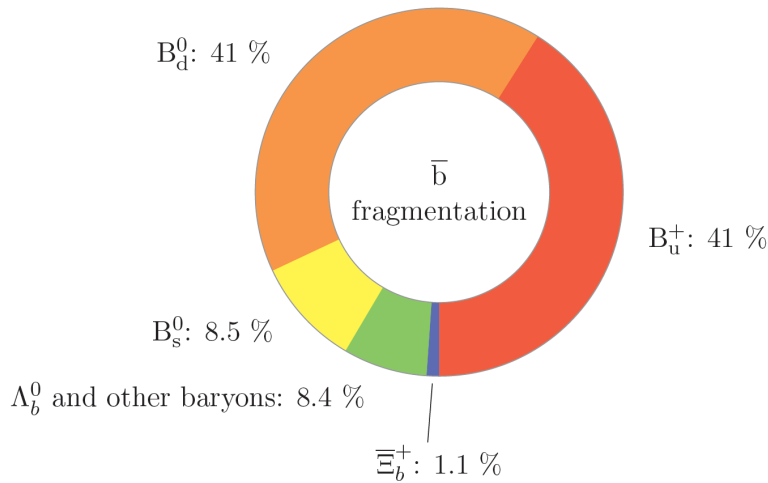


Figure 6.1: Beauty fragmentation as measured by the DELPHI Collaboration.[1]

## 6.2 Promising decay chains

The  $B^0$  meson decays before it reaches the detectors, so we need to find the meson by looking at its decay products. The  $B^0$  has a large number of decay channels of which we need to select one to perform our analysis. Most decay channels have a branching ratio that is too low to be measured. Only a few decay channels are promising for further study. Using data of the Particle Data group, We give an overview of these decay channels with their corresponding branching ratio's (BR)[22]:

### Full Hadronic Decays - $B^0 \rightarrow D^{*-} \dots \rightarrow D^0 \dots$

*First* - This is the decay channel we selected for the analysis in this thesis. It has a small number of final decay products, which limits the combinatorial background but it also has a small branching ratio, which means that we will need a lot of events to find a signal.

$$\begin{aligned} B^0 &\rightarrow D^{*-} \pi^+ & \text{BR} &= (2.76 \pm 0.13) \times 10^{-3} \\ D^{*-} &\rightarrow D^0 \pi^- & \text{BR} &= (67.7 \pm 0.5) \times 10^{-2} \\ D^0 &\rightarrow K^+ \pi^- & \text{BR} &= (3.89 \pm 0.05) \times 10^{-2} \end{aligned}$$

This results in the total process:

$$B^0 \rightarrow \pi^+ \pi^- \pi^- K^+ \quad \text{BR} = (7.27 \pm 0.36) \times 10^{-5}$$

*Second* - This channel has a branching ratio that is twice as high but the increase amount of end products could result in a combinatorial background that is too high and a larger amount of particles that are not detected by the detector.

$$\begin{aligned} B^0 &\rightarrow D^{*-} \pi^+ & \text{BR} &= (2.76 \pm 0.13) \times 10^{-3} \\ D^{*-} &\rightarrow D^0 \pi^- & \text{BR} &= (67.7 \pm 0.5) \times 10^{-2} \\ D^0 &\rightarrow K^+ \pi^- \pi^- \pi^+ & \text{BR} &= (8.07 \pm 0.23) \times 10^{-2} \end{aligned}$$

This results in the total process:

$$B^0 \rightarrow \pi^- \pi^- \pi^- \pi^+ \pi^+ K^+ \quad \text{BR} = (1.51 \pm 0.08) \times 10^{-4}$$

*Third* - This channel has a branching ratio that is two and a half times higher than the selected channel but it has a high chance that at least one of the end products will not lie in the acceptance of the detector.

$$\begin{aligned} B^0 &\rightarrow D^{*-} \pi^+ \pi^- \pi^+ & \text{BR} &= (7.0 \pm 0.8) \times 10^{-3} \\ D^{*-} &\rightarrow D^0 \pi^- & \text{BR} &= (67.7 \pm 0.5) \times 10^{-2} \\ D^0 &\rightarrow K^+ \pi^- & \text{BR} &= (3.89 \pm 0.05) \times 10^{-2} \end{aligned}$$

This results in the total process:

$$B^0 \rightarrow \pi^- \pi^- \pi^- \pi^+ \pi^+ K^+ \quad \text{BR} = (1.84 \pm 0.21) \times 10^{-4}$$

A combination of the changes in the second and the third channels would have the highest branching ratio ( $3.82 \times 10^{-4}$ ) but the total combinatorial background will probably be insurmountable. A possibility could be to select on the  $\rho^0$  resonances of these decays but this will also reduce the branching ratio to  $1.97 \times 10^{-4}$  with a large uncertainty.

### Full Hadronic Decays - $B^0 \rightarrow D^- \dots$

*First* - This decay channel has a high branching ratio and a limited amount of decay products which makes it a very promising decay channel for further analysis.

$$\begin{aligned} B^0 &\rightarrow D^- \pi^+ & \text{BR} &= (2.52 \pm 0.13) \times 10^{-3} \\ D^- &\rightarrow K^+ \pi^- \pi^- & \text{BR} &= (9.46 \pm 0.24) \times 10^{-2} \end{aligned}$$

This results in the total process:

$$B^0 \rightarrow \pi^+ \pi^- \pi^- K^+ \quad \text{BR} = (2.38 \pm 0.14) \times 10^{-4}$$

*Second* - This channel has a higher branching ratio but also a higher combinatorial background and a larger amount of particles that are not detected by the detector.

$$\begin{aligned} B^0 &\rightarrow D^- \pi^+ \pi^+ \pi^- & \text{BR} &= (6.0 \pm 0.7) \times 10^{-3} \\ D^- &\rightarrow K^+ \pi^- \pi^- & \text{BR} &= (9.46 \pm 0.24) \times 10^{-2} \end{aligned}$$

This results in the total process:

$$B^0 \rightarrow \pi^+ \pi^+ \pi^- \pi^- \pi^- K^+ \quad \text{BR} = (5.68 \pm 0.68) \times 10^{-4}$$

### Semi Leptonic Decays - $B^0 \rightarrow D^{*-} e^+ \nu_e \rightarrow D^0 \dots$

*First* - This decay channel has the highest branching ratio for a decay with four detectable end products. The neutrino is not detectable, which means that its properties have to be reconstructed. This introduces a large uncertainty in the final result.

$$\begin{aligned} B^0 &\rightarrow D^{*-} e^+ \nu_e & \text{BR} &= (4.93 \pm 0.11) \times 10^{-2} \\ D^{*-} &\rightarrow D^0 \pi^- & \text{BR} &= (67.7 \pm 0.5) \times 10^{-2} \\ D^0 &\rightarrow K^+ \pi^- & \text{BR} &= (3.89 \pm 0.05) \times 10^{-2} \end{aligned}$$

This results in the total process:

$$B^0 \rightarrow e^+ \nu_e \pi^- \pi^- K^+ \quad \text{BR} = (1.30 \pm 0.03) \times 10^{-3}$$

*Second* - Combinatorial background is a smaller issue for the semi leptonic decay channel while the uncertainty is a large problem. This channel could be interesting if it increases the momentum and decay vertex resolution of the reconstructed particles, leading to a smaller uncertainty in the neutrino reconstruction.

$$\begin{aligned} B^0 &\rightarrow D^{*-} e^+ \nu_e & \text{BR} &= (4.93 \pm 0.11) \times 10^{-2} \\ D^{*-} &\rightarrow D^0 \pi^- & \text{BR} &= (67.7 \pm 0.5) \times 10^{-2} \\ D^0 &\rightarrow K^+ \pi^- \pi^- \pi^+ & \text{BR} &= (8.07 \pm 0.23) \times 10^{-2} \end{aligned}$$

This results in the total process:

$$B^0 \rightarrow \pi^- \pi^- \pi^- \pi^+ \pi^+ K^+ \quad \text{BR} = (2.69 \pm 0.1) \times 10^{-3}$$

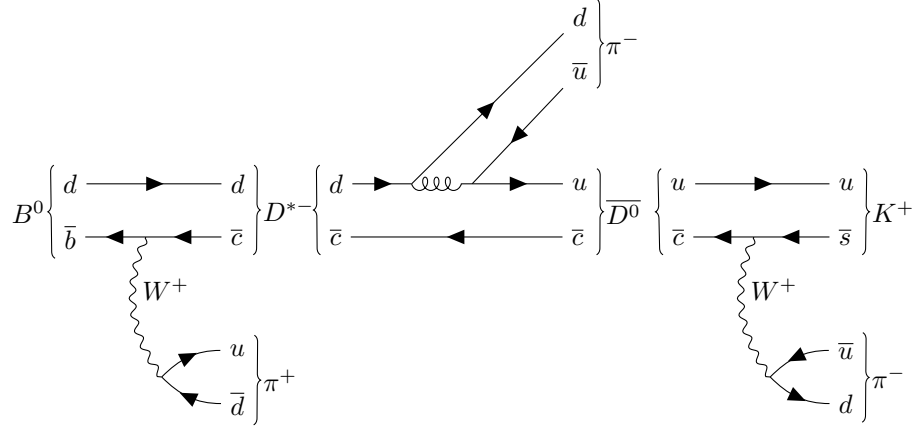


Figure 6.2: Feynman diagram for the full  $B^0$  decay we are studying

### 6.3 Expected $B^0$ production for selected decay chain

For the full hadronic reconstruction we will study the decay channel illustrated in figure 6.2 in more detail. Using the value for the branching ratio we can now calculate the number of  $B^0$  mesons that are produced in particle collisions.

#### 6.3.1 Number of $B^0$ mesons in pp collisions at $\sqrt{s} = 7$ TeV

We have two methods to calculate the number of  $B^0$  mesons that are expected to be produced. These only differ in the use of different literature values, which give slightly different values for the variables used in the calculation. The expected number of  $B^0$  mesons is given by the equation:

$$N_{B^0/\text{event}} = 2 \times f_{b \rightarrow B^0} \times N_{b\bar{b}/\text{event}}.$$

The fraction of beauty quarks that become a  $B^0$ ,  $f_{b \rightarrow B^0}$ , is 41%. The number of  $b\bar{b}$  quarks per event is given for 14 TeV pp collisions to be 0.006.[20] If we assume linear scaling of the number of produced quark pairs with the collision energy we get  $N_{b\bar{b}/\text{event}} = 0.003$  for pp collisions at 7 TeV. The factor of 2 in the equation is due to the creation of two beauty quarks that can both result in the creation of a  $B^0$  meson. This results in the estimate:

$$N_{B^0/\text{event}} = 2 \times 41\% \times 0.003 = 2.46 \times 10^{-3}.$$

For the second method we calculate the number of  $b\bar{b}$  quarks per event using a different literature value. We make use of the equation:

$$N_{pp} = \sigma_{pp}L \quad \text{and} \quad N_{b\bar{b}} = \sigma_{b\bar{b}}L,$$

where  $\sigma$  is the cross section and  $L$  is the integrated luminosity.  $N_{pp}$  is equal to the number of proton-proton collision events, therefore we can get the number of  $b\bar{b}$  quarks per event by dividing the two equations:

$$\frac{N_{b\bar{b}}}{N_{pp}} = \frac{\sigma_{b\bar{b}}}{\sigma_{pp}}$$

and setting  $N_{pp} = 1$ . For pp collisions at 7 TeV we find the cross sections  $\sigma_{b\bar{b}} = 429\mu\text{b}$ , and  $\sigma_{pp} = 98.6\text{mb}$ . [21] This gives the result:

$$N_{b\bar{b}/\text{event}} = \frac{429 \times 10^{-6}}{98.6 \times 10^{-3}} = 4.35 \times 10^{-3},$$

which gives

$$N_{B^0/\text{event}} = 2 \times 41\% \times 0.00435 = 3.57 \times 10^{-3}.$$



We can now calculate the number of  $B^0$  mesons with the correct decay channel will be produced. If we assume the lower expectation for the number of  $B^0$  mesons per event is correct we get:

$$N_{\text{Channel/event}} = N_{B^0/\text{event}} \times BR = 2.46 \times 10^{-3} \times 7.27 \times 10^{-5} = 1.79 \times 10^{-7}$$

So, we expect to produce 1.79  $B^0$  mesons with the selected decay channel or more per ten million events.

### 6.3.2 Number of $B^0$ mesons in p-Pb collisions at $\sqrt{s_{NN}} = 5.02$ TeV

For the calculation of the expected number of  $B^0$  mesons in p-Pb collisions we have to scale the results we obtained from the previous section. We have a higher number of collisions and a lower collision energy.

Table 6.1: Number of binary collisions as a function of centrality for p-Pb collisions at  $\sqrt{s_{NN}} = 5.02$  TeV.[9]

| Centrality (%) | $\langle N_{coll} \rangle$ |
|----------------|----------------------------|
| 0 - 5          | 14.7                       |
| 5 - 10         | 13.0                       |
| 10 - 20        | 11.7                       |
| 20 - 40        | 9.36                       |
| 40 - 60        | 6.42                       |
| 60 - 80        | 3.81                       |
| 80 - 100       | 1.94                       |
| 0 - 100        | 6.87                       |

If we take the number of binary collisions from table 6.1 for the full centrality range we get the number of  $B^0$  mesons per event:

$$N_{B^0/\text{event}} = 2 \times 41\% \times 0.003 \times \frac{5.02}{7} \times 6.87 = 12.12 \times 10^{-3},$$

which we can again use to calculate the expected number of  $B^0$  mesons with the correct decay channel:

$$N_{\text{Channel/event}} = N_{B^0/\text{event}} \times BR = 12.12 \times 10^{-3} \times 7.27 \times 10^{-5} = 8.8 \times 10^{-7}.$$

This means that we expect to find approximately five times as many  $B^0$  mesons with the correct decay channel in p-Pb events at 5.02 TeV compared to pp events at 7 TeV.

## Chapter 7

# $B^0$ - Reconstruction and Candidate Selection

### 7.1 Reconstruction

In order to reconstruct the  $B^0$  we have developed an analysis code that works in the ALICE computing framework. The reconstruction works for both simulated (Monte Carlo) and real data.

Collision events are loaded into the program, events that do not pass quality/trigger selection cuts are rejected. For Monte Carlo events we make a list of all particle tracks that belong to the correct decay chain so we fill separate histograms for signal and background. We use this data to apply cuts, which we will talk about in the next section.

After we have selected an event we select the tracks of all the final decay products of the decay channel that we are studying. We do this by applying a three sigma cut around the expected signal of each track in the TPC and the TOF detectors. We also require that each track has at least two hits in the ITS layers and at least one hit in the TPC. This requirement gets rid of misconstrued tracks.

Next, we take a pion and a kaon with opposite charges and propagate their tracks to their position of closest approach. This position will be the  $D^0$  decay vertex. We use this position and the properties of the pion and the kaon to reconstruct the  $D^0$  meson. Most of the reconstructed  $D^0$  candidates won't be real  $D^0$  mesons, so we apply cuts on the reconstructed particles that help to get rid of this background.

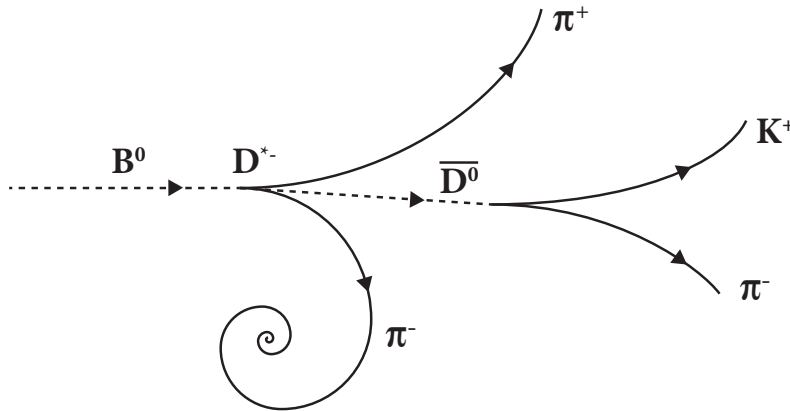


Figure 7.1: A sketch of the  $B^0 \rightarrow D^{*-} \pi^+ \rightarrow \bar{D}^0 \pi^- \pi^+ \rightarrow \pi^- K^+ \pi^- \pi^+$  decay.

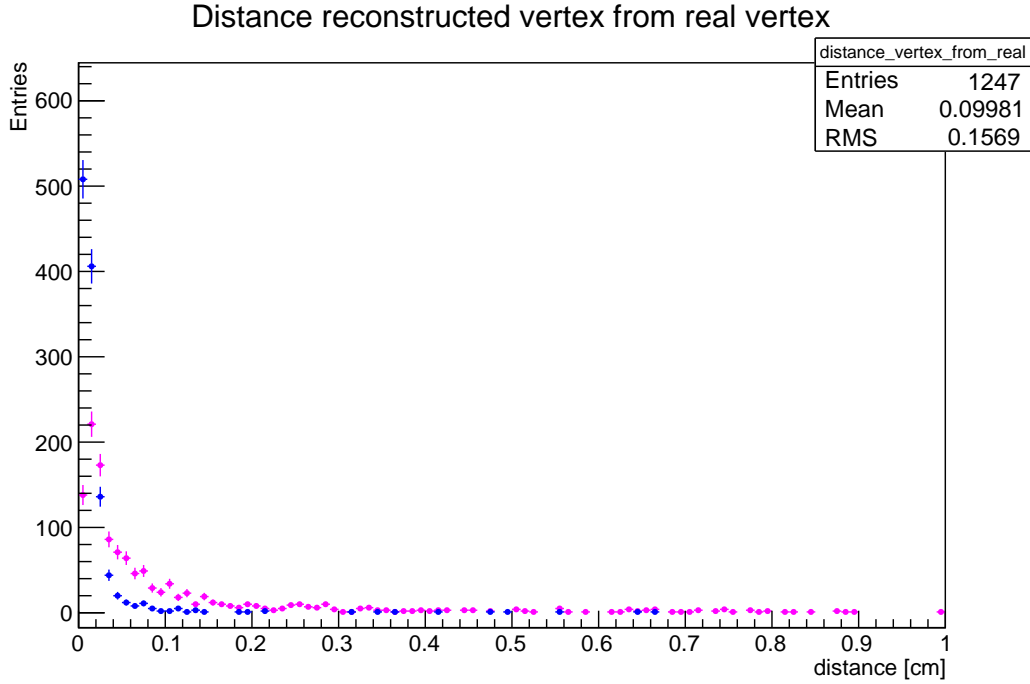


Figure 7.2: Original  $B^0$  vertex resolution in pink. Improved resolution in blue.

A logical next step would be to use the  $D^0$  track and the track of the  $D^*$  pion to find the  $D^*$  decay vertex. But if we do this we get a decay vertex position with a very large uncertainty. We found a workaround by using the fact that the  $D^*$  decays so fast that it has practically the same vertex position as the  $B^0$  (See figure 7.1). So we take the  $D^0$  track, the  $D^*$  pion track, and the  $B^0$  pion track and propagate all three tracks to their position of closest approach. This gives the decay vertex position for both the  $D^*$  and  $B^0$ . Both vertices are reconstructed with an improved vertex position, this is shown for the  $B^0$  in figure 7.2. The pp  $\sqrt{s} = 7$  TeV Monte Carlo data set LHC15a2a was used for this plot, and for all other plots in this chapter. More information about this data set can be found in chapter 8.

Using the  $D^*$  decay vertex position, we combine the properties of the  $D^0$  track and the  $D^*$  pion track into a  $D^*$  track. Next, we apply cuts on the reconstructed  $D^*$  track. The particles that pass this cut are then used along with the  $B^0$  pion to reconstruct the  $B^0$  track. Our final cuts are then applied on the  $B^0$  track.

At each step of combining the tracks we have to make sure that the charges of the tracks are correct. We also check that we don't use the same track twice. For the  $D^0$  we also have to make sure that it decays to a positive kaon and a negative pion when the  $D^*$  has a negative charge to prevent the inclusion of a different decay channel.

During the reconstruction all the information about the tracks is saved into histograms. In the next sections, we show some of these histograms. The final results are given in the next chapter.

### 7.1.1 Quality assessment

We check the quality of the reconstruction in three ways. First, we check the distance between the reconstructed decay vertices and the actual positions of these vertices. Second, we check the error in the reconstructed momenta of the particles. And lastly, we look at the reconstructed masses of the true signal particles. The error for the first two factors is given by  $\sigma = \sqrt{\Delta_x^2 + \Delta_y^2 + \Delta_z^2}$  using the difference in position and momentum respectively.

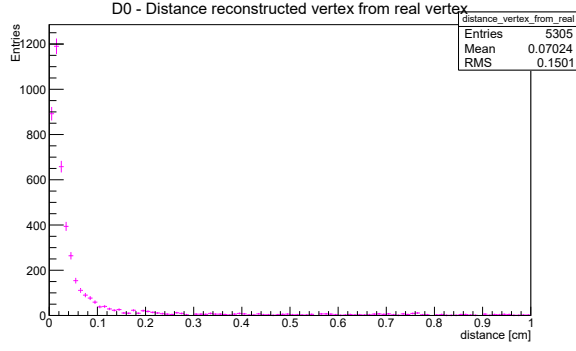


Figure 7.3: D0 decay vertex error.

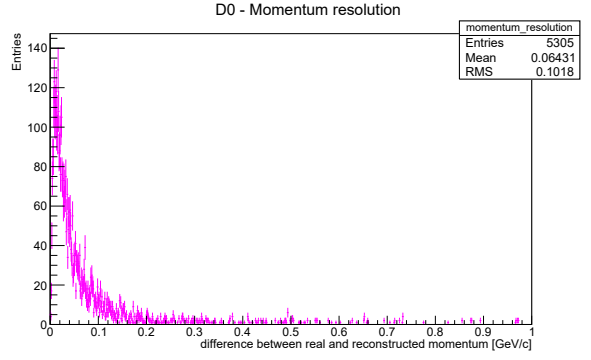


Figure 7.4: D0 momentum error.

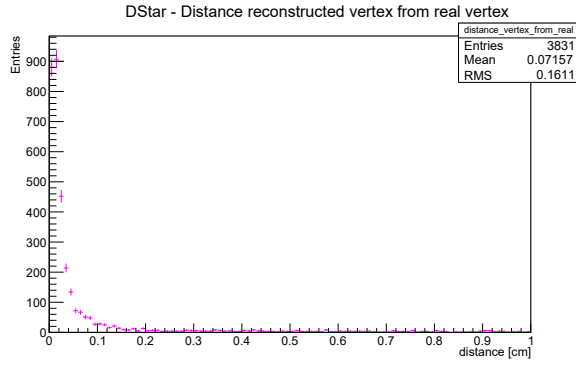


Figure 7.5: DStar decay vertex error.

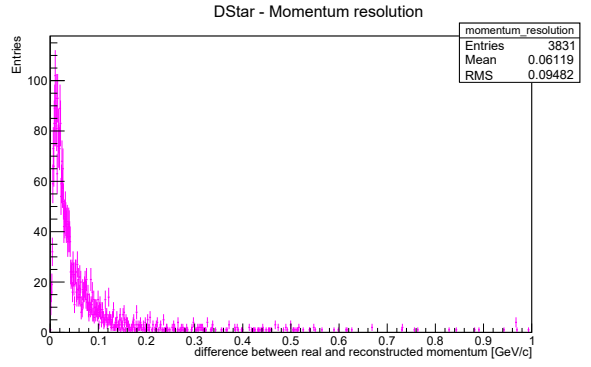


Figure 7.6: DStar momentum error.

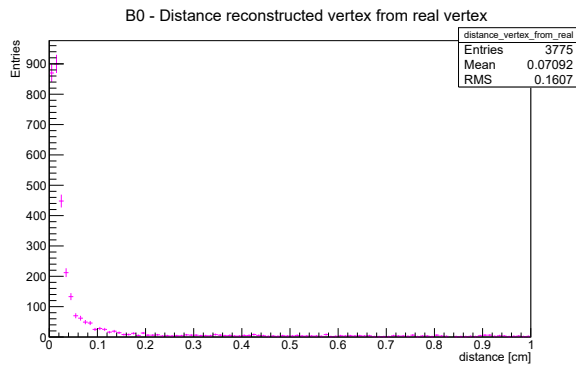


Figure 7.7: B0 decay vertex error.

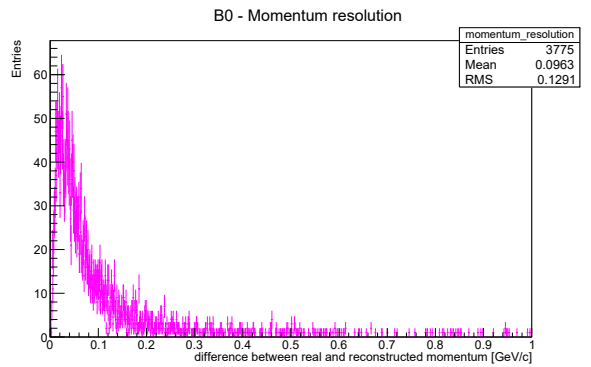


Figure 7.8: B0 momentum error.

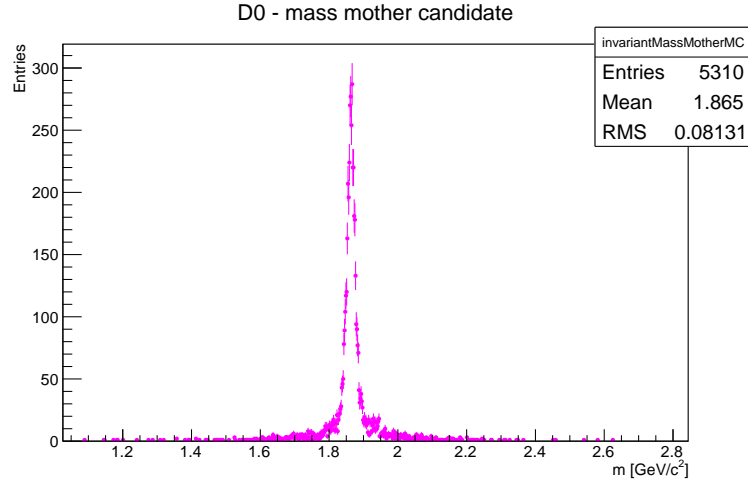


Figure 7.9: Reconstructed  $D^0$  mass for true  $D^0$  mesons.

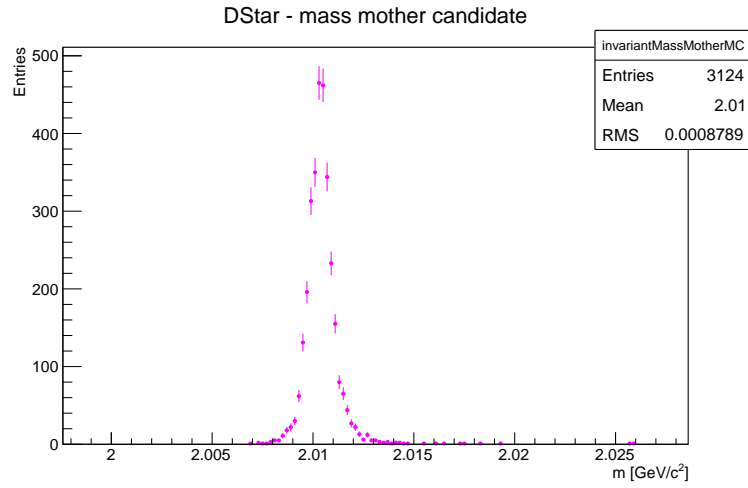


Figure 7.10: Reconstructed  $D^*$  mass for true  $D^*$  mesons.

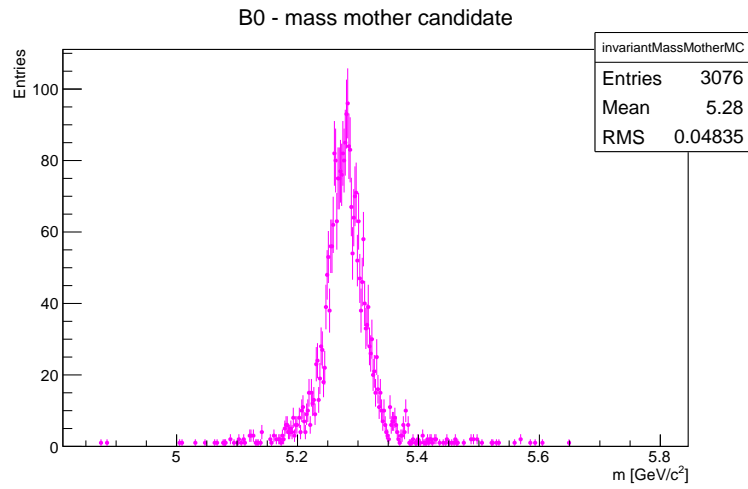


Figure 7.11: Reconstructed  $B^0$  mass for true  $B^0$  mesons.

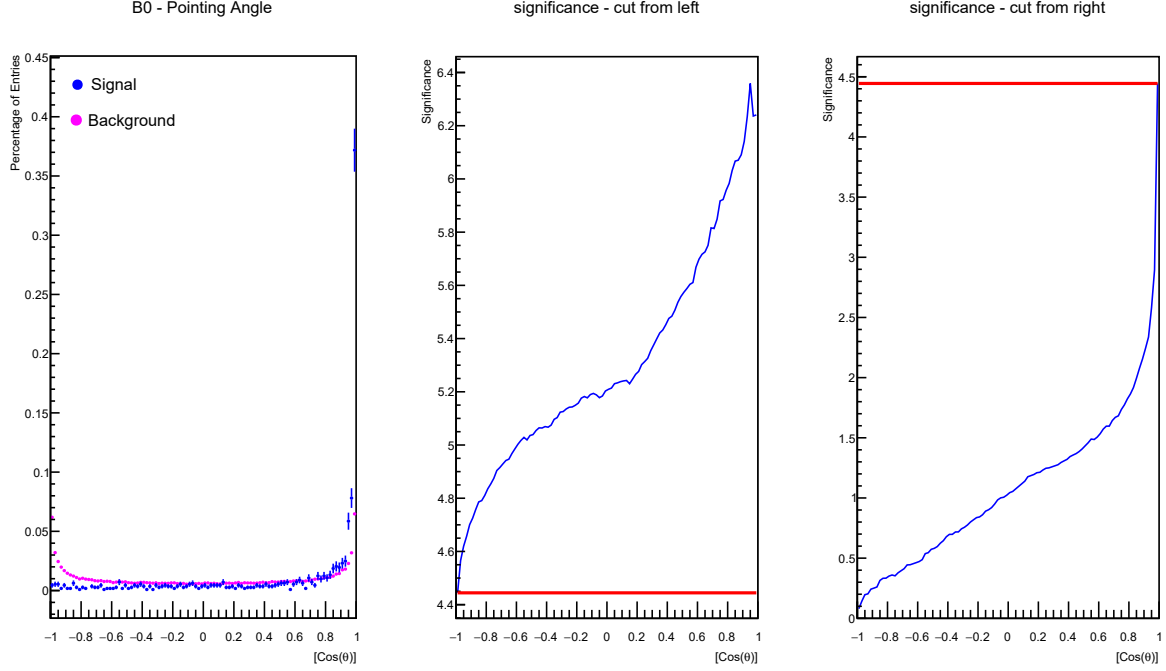


Figure 7.12: The left graph shows the pointing angle for both reconstructed signal and background  $B^0$  candidates with  $6 < p_T < 10$ . The number of entries are normalized to one for both sets. The middle and the right histogram are from a tool we developed that shows how a cut will affect the significance of the final result. The red line shows the current significance and the blue line the significance after applying a cut at that point.

For the QA results we have only used very loose cuts. The histograms in figure 7.3 till 7.11 show that the reconstruction is performed successfully with uncertainties in the vertex position and particle momentum resulting in widened mass peaks for the reconstructed particles.

## 7.2 Candidate selection

For the selection of signal candidates and the rejection of background candidates we have a number of cuts at our disposal. In this section, we give an overview of those cuts. Figure 7.12 shows the result for one of these cuts, the pointing angle, and the tool we use to determine the right cut value.

### Invariant mass window

An important cut that we apply is a cut on the invariant mass of reconstructed particles. We already know the mass that these particles have from other experiments. The invariant mass peak of these particles should be centered around their literature value with a Gaussian distribution due to imperfections in the momenta measurements of the daughter tracks and the uncertainty in the decay vertex reconstruction.

Using the Monte Carlo results we can determine the width of the invariant mass peak and remove candidates that are further than three sigma away from the central value.

Particles that are reconstructed with the use of a track that was reconstructed itself can have an improved invariant mass resolution by subtracting the invariant mass of the reconstructed daughter. This is called the delta invariant mass and it works because the uncertainty in the invariant mass of the reconstructed daughter is removed from the uncertainty in the invariant mass of the particle of interest. So, we also apply a three sigma cut on the delta invariant mass.

## Transverse momentum

The momentum perpendicular to the beam axis is called the transverse momentum  $p_T$ . The  $p_T$  distribution of particles coming from the QGP and subsequent particle decays is different from the  $p_T$  distribution of the particles that originate from our decay channel. We can use this fact to apply some cuts.

## Distance of closest approach

The distance of closest approach is the closest distance between two particle tracks. It is found by propagating the tracks through the magnetic field and finding the position where the tracks are closest to each other. If a particle decays, its daughters should originate from this position.

## Pointing angle

If we draw a line from the primary vertex (i.e. the collision point) to the decay vertex of a particle, we can calculate the angle between this vector and the momentum vector of the decayed particle. If the particle originates from the primary vertex we expect the pointing angle to be close to zero, while a random combination of particles is less likely to point in the same direction.

## Product of impact parameters

The impact parameter is the shortest distance with which a particle passes the primary vertex. It is found by calculating the path the particle travels through the magnetic field and finding the shortest distance between the path and the vertex. Particles that come from a decay should pass the vertex at a distance.

## Impact product

If a particle has two daughters we can multiply their impact parameters, this gives the impact product. The kinematics of a decay can lead to an asymmetry in the distribution of the impact product for signal particles.

## (Normalized) decay length

The decay length of a particle is the distance it travels from the point of production to the point of decay. All our reconstructed particles have a specific lifetime and will usually travel at relativistic speeds. Therefore the mean decay length should be comparable to  $d \approx c\tau$ , where  $c$  is the speed of light. We can apply a cut on the decay length to remove particles with a different decay length.

For the normalized decay length we take the error in the decay length measurement into account and apply a cut afterwards.

## Angle between daughter and mother

The angle between a particle and its decay products is kinematically constrained, so we can apply a cut on the angle.

## Cosine theta star

The cosine theta star is the cosine of the angle between the flight line of the mother and one of her daughters in the restframe of the mother.

## Topomatic cut

The topomatic cut is a cut that makes use of the fact that the impact parameter of a particle can be approximated with other observables. The errors in the measurements of these observables are also taken into account.

# Chapter 8

## Results

In this chapter, we present the results of the analyses in pp and p-Pb collisions. We use the results from Monte Carlo to give an estimate of the number of  $B^0$  we expect to find with the full hadronic reconstruction of the studied decay channel in data. After this, we present the results of the same analyses ran over real collision data. First, we will detail the data sets used and their properties. Then, we will show the results for the following analyses:

- **Monte Carlo simulations**

- Proton-Proton  $\sqrt{s} = 7$  TeV with an enhanced  $B^0$  meson signal
- Proton-Proton  $\sqrt{s} = 7$  TeV minimum bias
- Proton-Lead  $\sqrt{s_{NN}} = 5.02$  TeV with an enhanced  $B^0$  meson signal
- Proton-Proton  $\sqrt{s} = 7$  TeV with enhanced signal and simple EMCal trigger test

- **Real data**

- Proton-Proton  $\sqrt{s} = 7$  TeV
- Proton-Lead  $\sqrt{s_{NN}} = 5.02$  TeV

### 8.1 Data sets

For the analyses performed in the next sections we used both Monte Carlo and real data sets. First, we will look at the Monte Carlo data sets and then the data sets recorded by ALICE. We use Monte Carlo data sets that have an increased number of beauty quarks for the selection of the right cut values. We need this increased number of beauty quarks in order to gain enough statistics. If we do not have heavy flavor enriched samples, we would need a huge amount of events. This is because a handful of reconstructed particles does not show the distributions of the observables that we want to use to determine our cut values. The enhanced data sets shown in this section are enriched with one  $b\bar{b}$ -pair per two events.

The Monte Carlo data sets are generated to reflect the physical processes of interest as accurately as possible. Nevertheless, we need to keep in mind that these are simulations that are limited by both our understanding of the laws of the universe and the design choices that are made in the program that generates the simulation data. If our cuts, which are based on Monte Carlo data, are too strong we run the risk of suppressing deviations that occur in real data compared to Monte Carlo data.



## Proton-Proton $\sqrt{s} = 7$ TeV Monte Carlo - Enhanced

- Monte Carlo data set: LHC15a2a
- Proton-Proton collisions at  $\sqrt{s} = 7$  TeV
- PYTHIA heavy flavor enriched production anchored to pass4 reconstruction of pp 2010
- Data set contains approximately 31.8 million events
- We use about 28.7 million of these events after quality selection
- Number of B0's in all events  $\approx 12.4$  million  $\rightarrow 0.43$  B0/event
- Number of B0's of correct decay chain = 35.461
- Number of B0's with all four final tracks detected by ALICE = 3322

The events in the data set are grouped in separate runs. The runs used from this data set are shown in table 8.1:

Table 8.1: Run numbers for used  $\sqrt{s} = 7$  TeV pp Monte Carlo data set.

| Data set | Run numbers  |
|----------|--|
| LHC15a2a | 114786, 114798, 114918, 114920, 114924, 114930, 114931, 115186, 115193, 115310, 115318, 115322, 115328, 115335, 115345, 115393, 115399, 115401, 115414, 115521, 116079, 116081, 116102, 116288, 116402, 116403, 116562, 116571, 116574, 116643, 116645, 117048, 117050, 117052, 117053, 117059, 117060, 117063, 117092, 117099, 117109, 117112, 117116, 117220, 117222, 118506, 118507, 118512, 118518, 118556, 118558, 118560, 118561, 119159, 119161, 119163, 119841, 119842, 119844, 119845, 119846, 119849, 119853, 119856, 119859, 119862, 120067, 120069, 120072, 120073, 120076, 120079, 120244, 120503, 120504, 120505, 120616, 120617, 120671, 120741, 120750, 120758, 120820, 120821, 120822, 120823, 120824, 120825, 120829, 121039, 121040, 122374, 122375, 124751, 125023, 125083, 125085, 125097, 125100, 125101, 125133, 125134, 125139, 125140, 125156, 125186, 125295, 125296, 125628, 125630, 125632, 125633, 125842, 125843, 125844, 125847, 125848, 125849, 125850, 125851, 125855, 126004, 126007, 126008, 126073, 126078, 126081, 126082, 126088, 126090, 126097, 126158, 126160, 126167, 126168, 126283, 126284, 126285, 126350, 126351, 126352, 126359, 126403, 126404, 126405, 126406, 126407, 126408, 126409, 126422, 126424, 126425, 126432, 128366, 128452, 128486, 128494, 128495, 128498, 128503, 128504, 128505, 128506, 128582, 128590, 128592, 128594, 128596, 128605, 128609, 128611, 128615, 128621, 128677, 128678, 128777, 128778, 128819, 128820, 128823, 128824, 128833, 128834, 128835, 128836, 128843, 128850, 128853, 128855, 128913, 129042, 129512, 129513, 129514, 129515, 129516, 129519, 129520, 129521, 129523, 129524, 129525, 129527, 129528, 129536, 129540, 129586, 129587, 129599, 129639, 129641, 129647, 129650, 129651, 129652, 129653, 129659, 129666, 129723, 129725, 129726, 129729, 129734, 129735, 129736, 129738, 129742, 129744, 129959, 129960, 129961, 129962, 129966, 129983, 130149, 130151, 130157, 130158, 130168, 130172, 130178, 130342, 130343, 130354, 130356, 130358, 130360, 130375, 130479, 130480, 130481, 130517, 130519, 130520, 130524, 130526, 130601, 130608, 130609, 130620, 130621, 130623, 130628, 130696, 130704, 130793, 130795, 130798, 130799, 130802, 130803, 130804, 130834, 130840, 130842, 130844, 130847, 130848, 130850 |

## Proton-Proton $\sqrt{s} = 7$ TeV Monte Carlo - Minimum Bias

- Monte Carlo data set: LHC10f6a
- Proton-Proton collisions at  $\sqrt{s} = 7$  TeV
- PYTHIA minimum bias production anchored to LHC10d
- Data set contains approximately 149.5 million events
- We use about 114.1 million of these events after quality selection
- Number of B0's in all events  $\approx 0.7$  million  $\rightarrow 6 \times 10^{-3}$  B0/event
- Number of B0's of correct decay chain = 64
- Number of B0's with all four final tracks detected by ALICE = 5

Table 8.2: Run numbers for used  $\sqrt{s} = 7$  TeV pp minimum bias Monte Carlo data set.

| Data set | Run numbers  |
|----------|--|
| LHC10f6a | 122374, 122375, 124751, 125023, 125085, 125097, 125100, 125101, 125133, 125134, 125139, 125140, 125156, 125186, 125296, 125628, 125630, 125632, 125633, 125842, 125843, 125844, 125847, 125848, 125849, 125850, 125851, 125855, 126004, 126007, 126008, 126073, 126078, 126081, 126082, 126088, 126090, 126097, 126158, 126160, 126167, 126168, 126283, 126284, 126285, 126350, 126351, 126352, 126359, 126403, 126404, 126405, 126406, 126407, 126408, 126409, 126422, 126424, 126425, 126432, 126437 |

It is notable here that the number of  $B^0$  mesons per event appears to be about twice as high in minimum bias than expected based on our calculations in chapter 6. This warrants further study.

## Proton-Lead $\sqrt{s_{NN}} = 5.02$ TeV Monte Carlo - Enhanced

- Monte Carlo data set: LHC13d3\_plus
- Proton-Lead collisions at  $\sqrt{s_{NN}} = 5.02$  TeV
- PYTHIA heavy flavor enriched production anchored to LHC13b,c
- Dataset contains approximately 37.3 million events
- We use about 31.6 million of these events after quality selection
- Number of B0's in all events  $\approx 14.4$  million  $\rightarrow 0.46$  B0/event
- Number of B0's of correct decay chain = 9614
- Number of B0's with all four final tracks detected by ALICE = 1867

Table 8.3: Run numbers for used  $\sqrt{s_{NN}} = 5.02$  TeV p-Pb Monte Carlo data set.

| Data set     | Run numbers  |
|--------------|--|
| LHC13d3_plus | 195389, 195390, 195391, 195478, 195479, 195480, 195481, 195482, 195483, 195529, 195531, 195566, 195567, 195568, 195592, 195593, 195633, 195635, 195644, 195673, 195675, 195677 |

## Proton-Proton $\sqrt{s} = 7$ TeV Real Data

- Data set: LHC10b,c,d,e
- Proton-Proton collisions at  $\sqrt{s} = 7$  TeV
- Data recorded by ALICE in 2010
- Data set contains approximately 446.6 million events
- We use about 318.6 million of these events after quality selection
- Expected number of  $B^0$ 's in all events  $\approx 0.8$  million
- Expected number of  $B^0$ 's of correct decay chain  $\approx 57$

The expected number that we can detect is the number of  $B^0$  mesons of the correct decay chain multiplied by the acceptance of the detector and the efficiency of the reconstruction. We will obtain these values using the Monte Carlo data sets.

Table 8.4: Run numbers for used  $\sqrt{s} = 7$  TeV pp data sets.

| Data set | Run numbers  |
|----------|--|
| LHC10b   | 117222, 117220, 117116, 117112, 117109, 117099, 117092, 117086, 117077, 117065, 117063, 117060, 117059, 117054, 117053, 117052, 117050, 117048, 116645, 116643, 116574, 116571, 116562, 116403, 116288, 116102, 115401, 115393, 115193, 115186, 114931   |
| LHC10c   | 120829, 120825, 120824, 120823, 120822, 120821, 120820, 120758, 120750, 120741, 120671, 120617, 120616, 120505, 120504, 120503, 120244, 120079, 120076, 120073, 120072, 120069, 120067, 119862, 119859, 119856, 119853, 119849, 119846, 119845, 119844, 119842, 119841, 119163, 119161, 119159   |
| LHC10d   | 126437, 126432, 126425, 126424, 126422, 126409, 126408, 126407, 126406, 126405, 126404, 126403, 126359, 126352, 126351, 126285, 126284, 126283, 126168, 126160, 126158, 126097, 126090, 126088, 126082, 126081, 126078, 126073, 126008, 126007, 126004, 125855, 125851, 125850, 125849, 125848, 125847, 125844, 125843, 125842, 125633, 125632, 125630, 125296, 125134, 125101, 125100, 125097, 125085, 125023, 124751, 122375, 122374   |
| LHC10e   | 130840, 130834, 130848, 130847, 130844, 130842, 130799, 130798, 130795, 130793, 130704, 130696, 130608, 130601, 130520, 130519, 130517, 130480, 130375, 130356, 130354, 130343, 130342, 130179, 130178, 130172, 130158, 130157, 130149, 129983, 129961, 129960, 129959, 129744, 129742, 129738, 129736, 129735, 129729, 129726, 129725, 129723, 129667, 129666, 129659, 129654, 129653, 129652, 129650, 129647, 129641, 129639, 129599, 129587, 129586, 129540, 129528, 129527, 129523, 129520, 129514, 129513, 129512, 128913, 128855, 128853, 128850, 128843, 128836, 128835, 128833, 128824, 128823, 128820, 128778, 128777, 128678, 128677, 128621, 128615, 128611, 128609, 128605, 128582, 128507, 128505, 128504, 128503, 128498, 128495, 128494, 128486, 128483, 128452, 128366, 128263, 128260, 128192, 128191, 128189, 128186, 128185, 127942, 127941, 127940, 127937, 127936, 127935, 127933, 127931, 127822, 127719, 127718, 127714, 127712 |

### Proton-Lead $\sqrt{s_{NN}} = 5.02$ TeV Real Data

- Data set: LHC13b,c
- Proton-Lead collisions at  $\sqrt{s_{NN}} = 5.02$  TeV
- Data recorded by ALICE in 2013
- Data set contains approximately 110.2 million events
- We use about 93.6 million of these events after quality selection
- Expected number of B0's in all events  $\approx 1.13$  million
- Expected number of B0's of correct decay chain  $\approx 82.4$

Table 8.5: Run numbers for used  $\sqrt{s_{NN}} = 5.02$  TeV p-Pb data sets.

| Data set | Run numbers  |
|----------|--|
| LHC13b   | 195483, 195482, 195481, 195480, 195479, 195478, 195391, 195390, 195389, 195351, 195346, 195344                                 |
| LHC13c   | 195677, 195676, 195675, 195673, 195644, 195635, 195633, 195596, 195593, 195592, 195568, 195567, 195566, 195532, 195531, 195529 |

## 8.2 Results for pp collisions at $\sqrt{s} = 7$ TeV

### 8.2.1 Monte Carlo Simulation

We performed our analysis on the heavy flavor enhanced data set LHC15a2a. For this analysis we used the following cuts:

Cuts per  $B^0$   $p_T$  bin [GeV/c]

|   |   | $0 < p_T < 3$ | $3 < p_T < 6$ | $6 < p_T < 10$ | $10 < p_T < 18$ | $18 < p_T < 30$ |
|---|---|---------------|---------------|----------------|-----------------|-----------------|
| <b><math>B^0</math></b>                     |   |               |               |                |                 |                 |
| DCA [cm]                                    | > | 0.025         | 0.03          | 0.03           | 0.03            | 0.05            |
| Norm. dec. length [a.u.]                    | < | -             | 2.0           | 2.0            | 1.0             | -               |
| Pointing Angle [ $\cos(\theta)$ ]           | < | 0.0           | 0.85          | 0.85           | 0.9             | 0.9             |
| Impact parameter [cm]                       | < | -             | 0.004         | 0.003          | 0.003           | 0.00225         |
| Imp. Product [ $\text{cm}^2$ ]              | > | -             | 0.0           | 0.0            | 0.0             | 0.0             |
| Pt B0 Pion daughter [GeV/c]                 | < | 1.0           | 1.25          | 1.25           | 1.25            | 1.5             |
| <b><math>D^*</math></b>                     |   |               |               |                |                 |                 |
| Inv. mass window $D^*$ [ $\text{GeV}/c^2$ ] | = | 0.00266       | 0.00266       | 0.00266        | 0.00266         | 0.00266         |
| $ \cos(\theta^*) $ $D^0$ daughter [cm]      | < | 0.45          | -             | -              | -               | -               |
| Transverse momentum [GeV/c]                 | < | 1.3           | 1.3           | 1.3            | 1.3             | 1.3             |
| <b><math>D^0</math></b>                     |   |               |               |                |                 |                 |
| Inv. mass window [ $\text{GeV}/c^2$ ]       | = | 0.04          | 0.045         | 0.045          | 0.05            | 0.075           |
| DCA [cm]                                    | > | 0.1           | 0.1           | 0.1            | 0.1             | 0.1             |
| Pointing Angle [ $\cos(\theta)$ ]           | < | 0.0           | 0.0           | 0.4            | 0.6             | 0.8             |
| Impact parameter [cm]                       | < | -             | 0.004         | 0.003          | 0.003           | 0.00225         |
| decay length/ $P_{D^0}$ [cm c/GeV]          | < | -             | 0.05          | 0.05           | 0.05            | -               |
| Transverse momentum [ $\text{GeV}/c^2$ ]    | < | 1.2           | 1.2           | 1.2            | 1.2             | 1.2             |

Additionally, we use the PID and quality selection cuts for the tracks as described in chapter 7.1. Using these settings we get the invariant mass distributions shown in figure 8.1 till 8.3. In the invariant mass plots we show the mass of the reconstructed  $B^0$  minus the mass of the reconstructed  $D^0$ . We do this because this removes part of the uncertainty in the invariant mass reconstruction, which results in a sharper peak.

We also add a cut on the combined number of TPC clusters ( $N_{TPC} < 400$ ) that were activated by the final tracks of the  $B^0$  decay. This cuts away more background than signal. The signal that is cut also has a lower quality on average than the the signal with more hits in the TPC.

The background is fitted by an exponential and the signal is fitted by a Gaussian. The graphs in figure 8.1 show the results per  $p_T$  bin and for the full  $p_T$  integrated range. It is clear that the first  $p_T$  bin ( $0 < p_T < 3$  [GeV/c]) is the least successful in separating background from signal. In figure 8.2 we show the same invariant mass histograms for the  $p_T$  integrated range starting from a  $p_T$  of 3 and 6 [GeV/c] respectively. These histograms show the clearest signal, so the chance to see a sign of the  $B^0$  using this decay channel in real data will be highest for these  $p_T$  ranges.

In the left graph of figure 8.3 we can see the masses per  $p_T$  bin and the uncertainty in the mass along with the Particle Data Group (PDG) value for the mass. Again we use the mass of the  $B^0$  minus the mass of the  $D^0$ . In the right graph we see the uncertainty in the invariant mass peak width.

Figure 8.4 shows the acceptance times efficiency per  $p_T$  bin for the  $B^0$  detection and reconstruction.

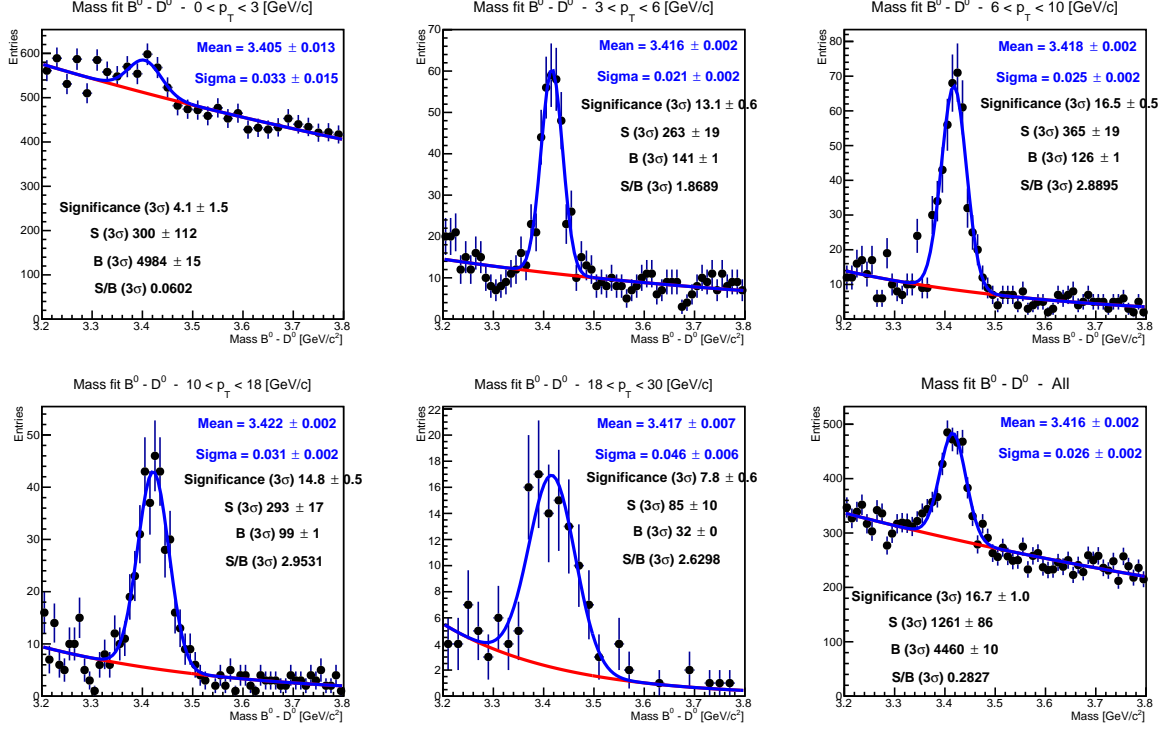


Figure 8.1: The invariant mass distributions for the reconstructed  $B^0$  candidates per  $p_T$  bin. The invariant mass of the  $D^0$  is subtracted to reduce the peak width. The background is fitted by an exponential (red line) and the signal is fitted by a Gaussian (blue line).

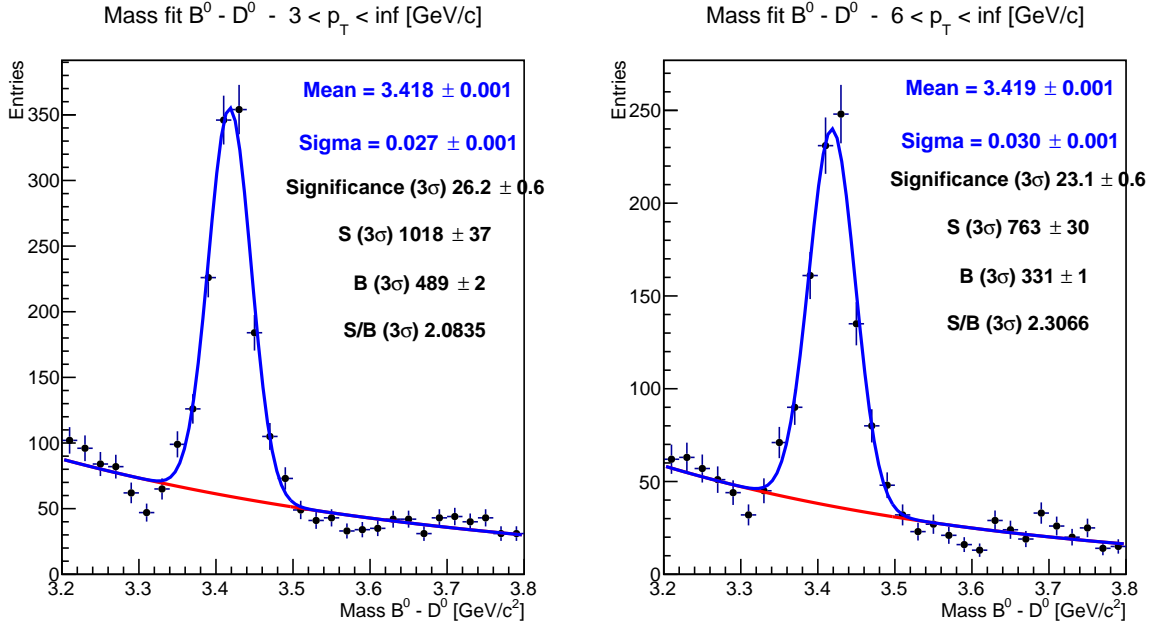


Figure 8.2: The invariant mass distributions for the reconstructed  $B^0$  candidates per  $p_T$  bin. The invariant mass of the  $D^0$  is subtracted to reduce the peak width. The background is fitted by an exponential (red line) and the signal is fitted by a Gaussian (blue line).

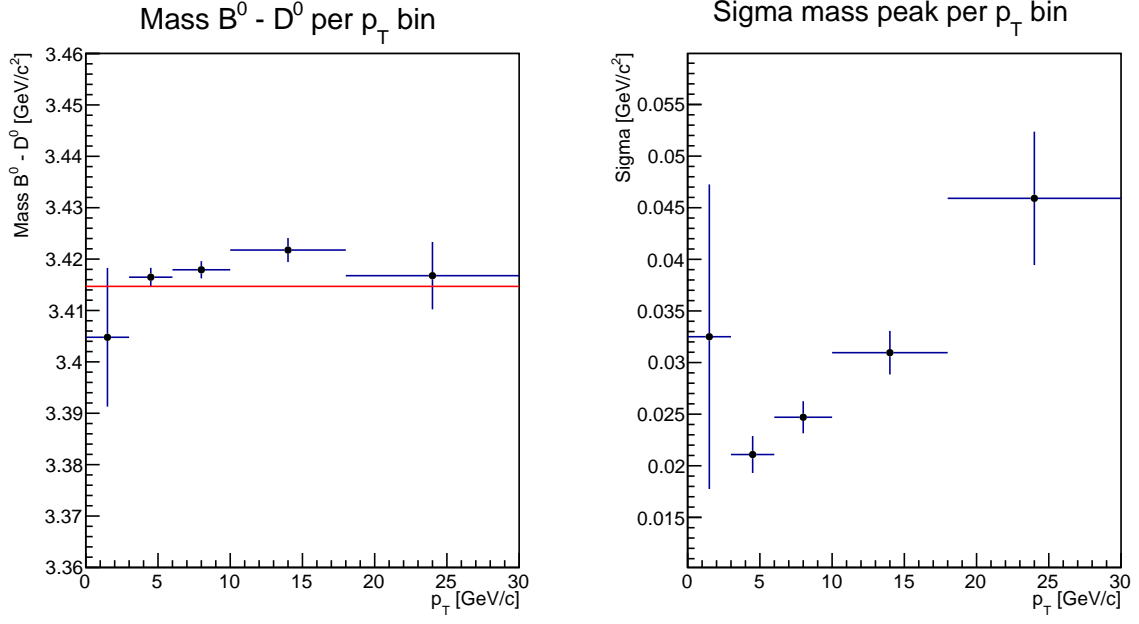


Figure 8.3: The left graph shows the mean of the invariant mass peaks of the reconstructed  $B^0$  candidates minus the invariant mass of the  $D^0$  per  $p_T$  bin. The red line shows the PDG value of the mass  $B^0 - D^0$ . The right graph shows the width of the invariant mass peaks per  $p_T$  bin.

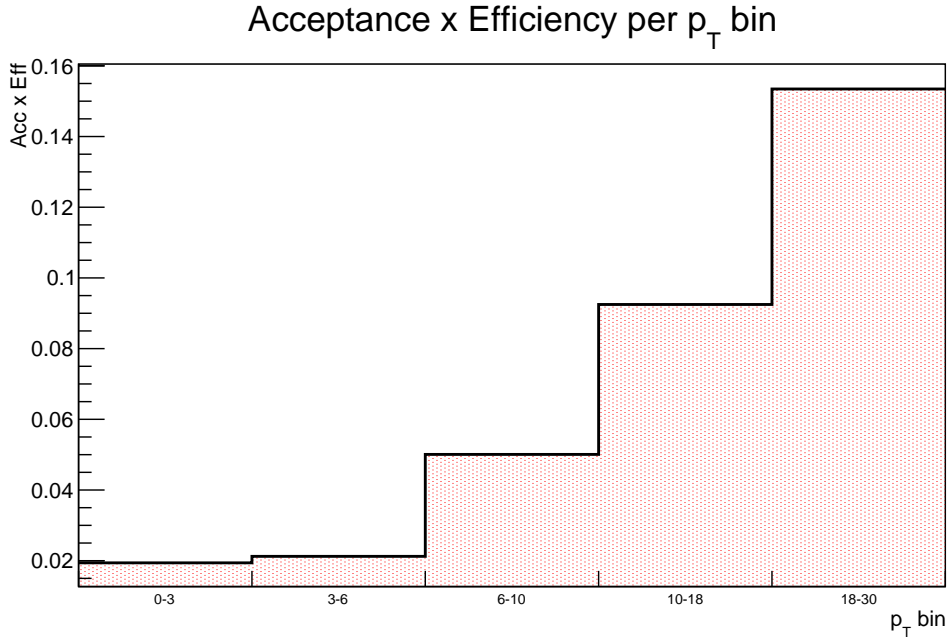


Figure 8.4: Acceptance times the efficiency per  $p_T$  bin for  $B^0$  detection and reconstruction in Monte Carlo pp collisions at  $\sqrt{s} = 7$  TeV.

### 8.2.2 Expectation in Data

We want to know the total number of  $B^0$  mesons that we expect to find in real data of pp collisions. In order to calculate this number we look at the efficiency of reconstructing the decay channel of the  $B^0$  in Monte Carlo and the expected number of  $B^0$  mesons generated in data. Using these numbers we should be able to calculate the number of expected  $B^0$  mesons that we should measure in data.

#### Efficiency of reconstruction in Monte Carlo

Using the Monte Carlo data set LHC15a2a we have approximately 28 million events containing an enhanced number of  $B^0$ . In order to ignore the possible effects caused by forcing of specific decay channels we only look at the total number of  $B^0$  mesons that decay with the correct decay branch.

In total, there are 35461  $B^0 \rightarrow \pi^+\pi^-\pi^-K^+$  created in the Monte Carlo data set. Of these there are 3322 of which all the final tracks are measured. So we find:

$$\text{Acc} = \frac{3322}{35461} = 9.37\%.$$

Next, we need to calculate the efficiency of the reconstruction. Of the 3322  $B^0 \rightarrow \pi^+\pi^-\pi^-K^+$  we manage to reconstruct 1330  $B^0$  mesons after using cuts. This results in the efficiency for the full  $p_T$  range:

$$\text{Eff} = \frac{1330}{3322} = 40.0\%,$$

which gives us the factor for the full  $p_T$  range:

$$\text{Acc} \times \text{Eff} = 9.37\% \times 40.0\% = 3.75\%.$$

#### Number of $B^0$ mesons expected in measurement pp 7 TeV data

Using these results we find the number of  $B^0 \rightarrow \pi^+\pi^-\pi^-K^+$  we expect to find in data per event:

$$N_{\text{Channel/event}} = N_{B^0/\text{event}} \times \mathbf{BR} \times \text{Acc} \times \text{Eff}.$$

We found two literature values for beauty quark production in chapter 6.3. The number of  $B^0$  mesons per event we find for the first and for the second value respectively are:

$$N_{\text{Channel/event}} = 2.46 \times 10^{-3} \times 7.27 \times 10^{-5} \times 3.75\% = \mathbf{6.71 \times 10^{-9}},$$

$$N_{\text{Channel/event}} = 3.57 \times 10^{-3} \times 7.27 \times 10^{-5} \times 3.75\% = \mathbf{9.73 \times 10^{-9}}.$$

If we instead assume an efficiency of 100% we get:

$$N_{\text{Channel/event}} = 2.46 \times 10^{-3} \times 7.27 \times 10^{-5} \times 9.37\% = \mathbf{16.76 \times 10^{-9}},$$

$$N_{\text{Channel/event}} = 3.57 \times 10^{-3} \times 7.27 \times 10^{-5} \times 9.37\% = \mathbf{24.32 \times 10^{-9}}.$$

This means that the total number of  $B^0$  mesons we can measure using this decay branch is approximately 24 per one billion events if we have a perfect efficiency. This means that there is room for improvement by obtaining a higher efficiency. Realistically the efficiency will probably not reach 100% so the number of  $B^0$  mesons we can measure will be lower than 24 per one billion event. Using the same calculation we show the expected number of  $B^0$  mesons per billion events per  $p_T$  bin in figure 8.5. We used the lower estimate for beauty production for this calculation.



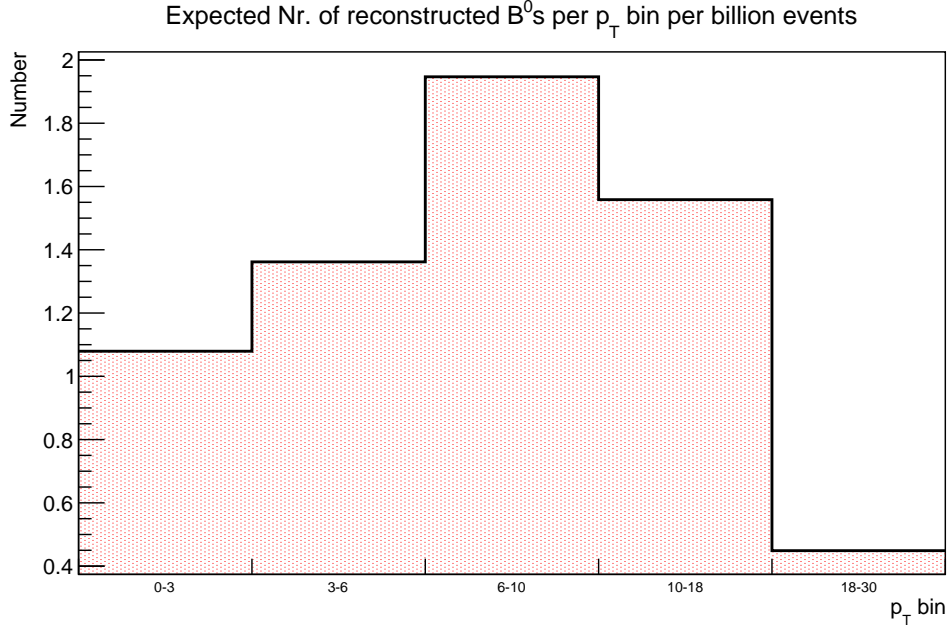


Figure 8.5: Using the reconstruction efficiency and the  $B^0$  production per  $p_T$  bin we get the average number of  $B^0$  we expect to find in one billion pp collision events at  $\sqrt{s} = 7$  TeV.

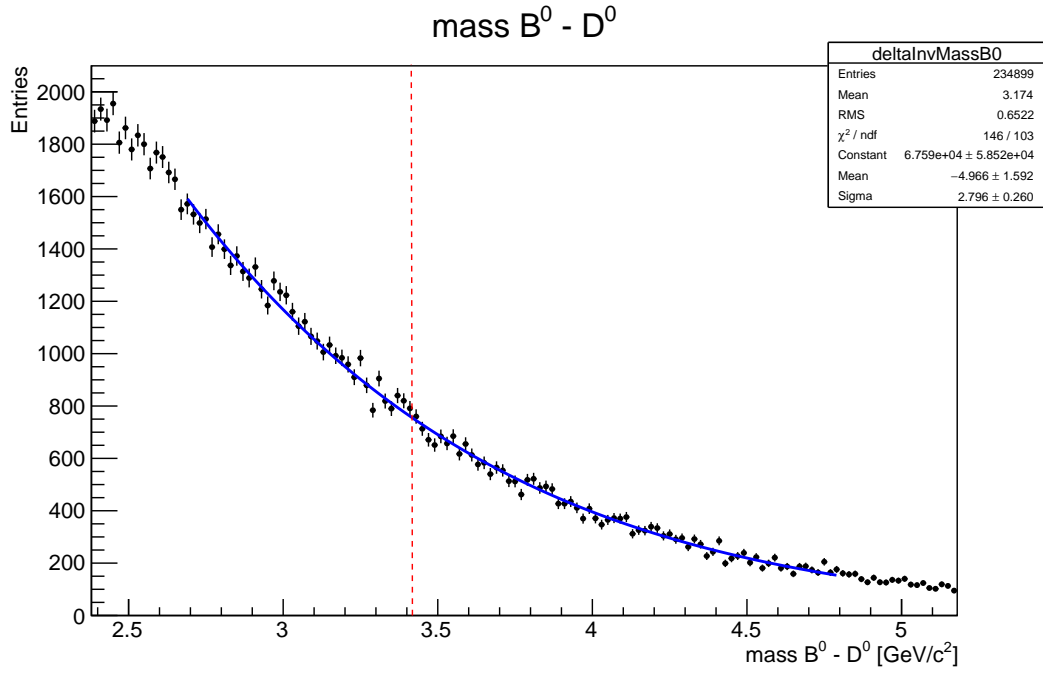


Figure 8.6: This graph shows the  $B^0 - D^0$  invariant mass result for the  $B^0$  candidates in real pp collisions at  $\sqrt{s} = 7$  TeV. The blue line shows an exponential fit of the background. The red dotted line show the PDG value for the  $B^0 - D^0$  mass.

### 8.2.3 Data

We use the data sets LHC10b,c,d, and e. We have 318.6 million pp  $\sqrt{s} = 7$  TeV events, this means that we expect to measure:

$$N_{\text{Channel}} = N_{\text{Channel/event}} \times N_{\text{events}} = 6.71 \times 10^{-9} \times 318.6 \times 10^6 = 2.14$$

Where we use the conservative beauty production calculation. We thus find that we can expect to measure about 2  $B^0$  mesons in these data sets. This number is too low to differentiate signal from background because the deviation in the background is larger than this number. This can be seen in the  $p_T$  integrated results shown in figure 8.6. We used the same cuts that were used for the Monte Carlo analysis.

### 8.2.4 Minimum Bias

We performed an analysis on the minimum bias data set LHC10f6a using the same settings as the Monte Carlo analysis for pp collisions at  $\sqrt{s} = 7$  TeV. There are a total of five  $B^0$  mesons of which all tracks are detected by the detector. One  $B^0$  passes all the cuts during reconstruction.

## 8.3 Results for p-Pb collisions at $\sqrt{s_{NN}} = 5.02$ TeV

### 8.3.1 Monte Carlo Simulation

We performed our analysis on the heavy-flavor enhanced data set LHC13d3\_plus. Like the analysis from the previous section, we used the track selection cuts from chapter 7.1 and a cut on the total hits of the four daughter tracks in the TPC of  $N_{TPC} < 400$ . The results of this analysis are shown in figures 8.7 to 8.10. For this analysis, we used the following cuts:

Cuts per  $B^0$   $p_T$  bin [GeV/c]

|  |   | $0 < p_T < 3$ | $3 < p_T < 6$ | $6 < p_T < 10$ | $10 < p_T < 18$ | $18 < p_T < 30$ |
|--|---|---------------|---------------|----------------|-----------------|-----------------|
| <b><math>B^0</math></b>                      |   |               |               |                |                 |                 |
| DCA [cm]                                     | > | 0.025         | 0.03          | 0.03           | 0.03            | 0.05            |
| Norm. dec. length [a.u.]                     | < | 2.0           | 3.0           | 3.0            | 3.5             | 3.5             |
| Pointing Angle [cos( $\theta$ )]             | < | 0.8           | 0.9           | 0.85           | 0.9             | 0.9             |
| Impact parameter [cm]                        | > | 0.015         | 0.015         | 0.015          | 0.015           | 0.015           |
| Impact parameter Pion [cm]                   | < | 0.015         | 0.015         | 0.005          | 0.005           | -               |
| Imp. Product [cm <sup>2</sup> ]              | > | -0.0002       | -0.0001       | -0.0001        | -0.0001         | 0.0             |
| $p_T$ B0 Pion daughter [GeV/c]               | < | 0.6           | 0.6           | 0.6            | 0.6             | 0.6             |
| <b><math>D^*</math></b>                      |   |               |               |                |                 |                 |
| Inv. mass window $D^*$ [GeV/c <sup>2</sup> ] | = | 0.00266       | 0.00266       | 0.00266        | 0.00266         | 0.00266         |
| DCA [cm]                                     | > | 0.1           | 0.1           | 0.1            | 0.1             | 0.1             |
| cos( $\theta^*$ )  $D^0$ daughter [cm]       | < | 0.45          | -             | -              | -               | -               |
| Pointing Angle [cos( $\theta$ )]             | < | -             | 0.5           | 0.6            | 0.8             | 0.9             |
| Impact parameter $D^0$ [cm]                  | < | -             | 0.004         | 0.003          | 0.003           | 0.0025          |
| Transverse momentum [GeV/c]                  | < | 1.3           | 1.3           | 1.3            | 1.3             | 1.3             |
| <b><math>D^0</math></b>                      |   |               |               |                |                 |                 |
| Inv. mass window [GeV/c <sup>2</sup> ]       | = | 0.04          | 0.045         | 0.045          | 0.05            | 0.075           |
| DCA [cm]                                     | > | 0.04          | 0.04          | 0.1            | 0.04            | 0.04            |
| Norm. dec. length [a.u.]                     | < | 3.0           | 3.0           | -              | -               | -               |
| Pointing Angle [cos( $\theta$ )]             | < | 0.0           | 0.0           | 0.6            | 0.8             | 0.9             |
| Impact parameter [cm]                        | < | -             | 0.004         | 0.003          | 0.003           | 0.00225         |
| decay length/ $P_{D^0}$ [cm c/GeV]           | < | -             | 0.05          | 0.05           | 0.05            | -               |
| Transverse momentum [GeV/c]                  | < | 1.5           | 1.5           | 1.5            | 1.5             | 1.5             |
| Angle D0 Pion [cos( $\theta$ )]              | < | -0.2          | -             | -              | -               | -               |

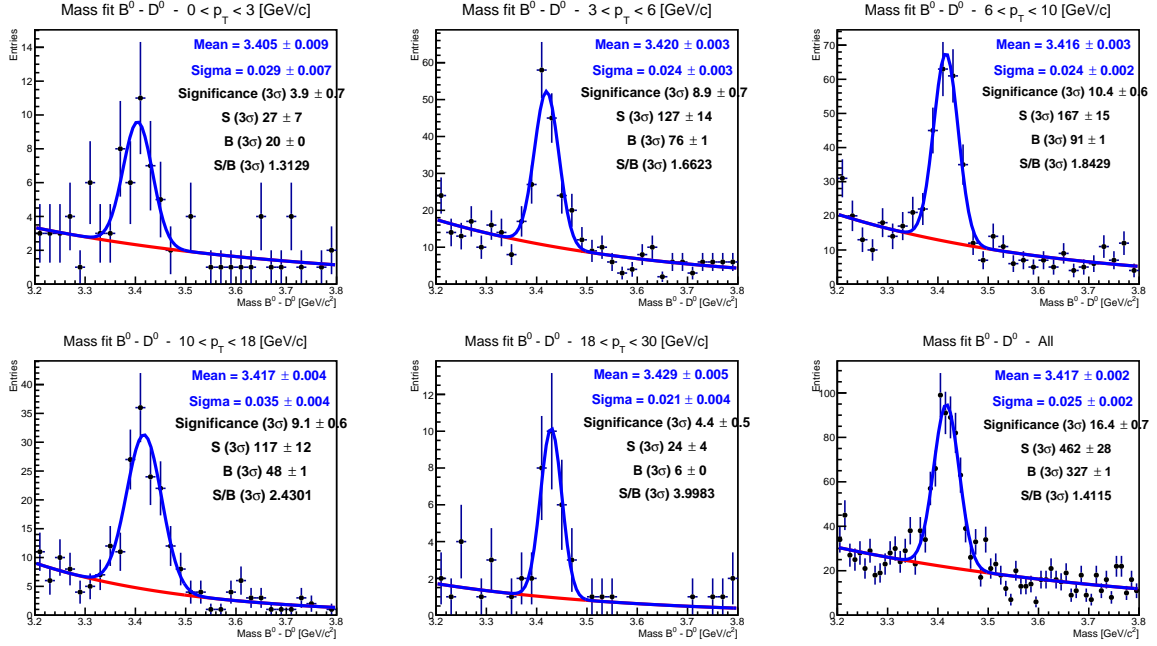


Figure 8.7: The invariant mass distributions for the reconstructed  $B^0$  candidates per  $p_T$  bin. The invariant mass of the  $D^0$  is subtracted to reduce the peak width. The background is fitted by an exponential (red line) and the signal is fitted by a Gaussian (blue line).

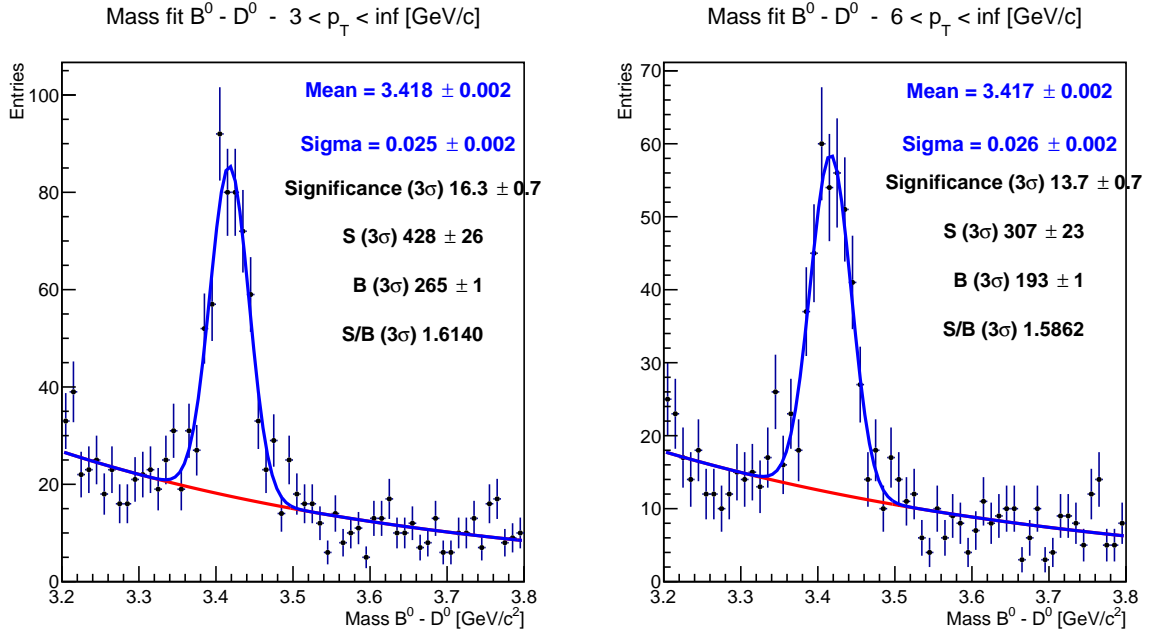


Figure 8.8: The invariant mass distributions for the reconstructed  $B^0$  candidates per  $p_T$  bin. The invariant mass of the  $D^0$  is subtracted to reduce the peak width. The background is fitted by an exponential (red line) and the signal is fitted by a Gaussian (blue line).

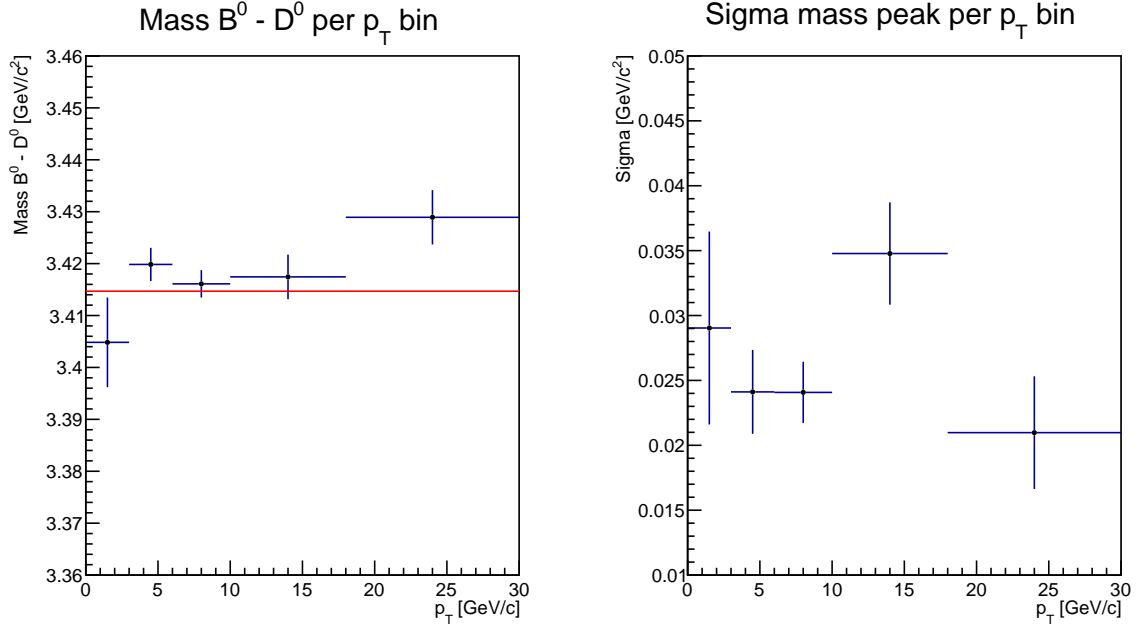


Figure 8.9: The left graph shows the mean of the invariant mass peaks of the reconstructed  $B^0$  candidates minus the invariant mass of the  $D^0$  per  $p_T$  bin. The red line shows the PDG value of the mass  $B^0 - D^0$ . The right graph shows the width of the invariant mass peaks per  $p_T$  bin.

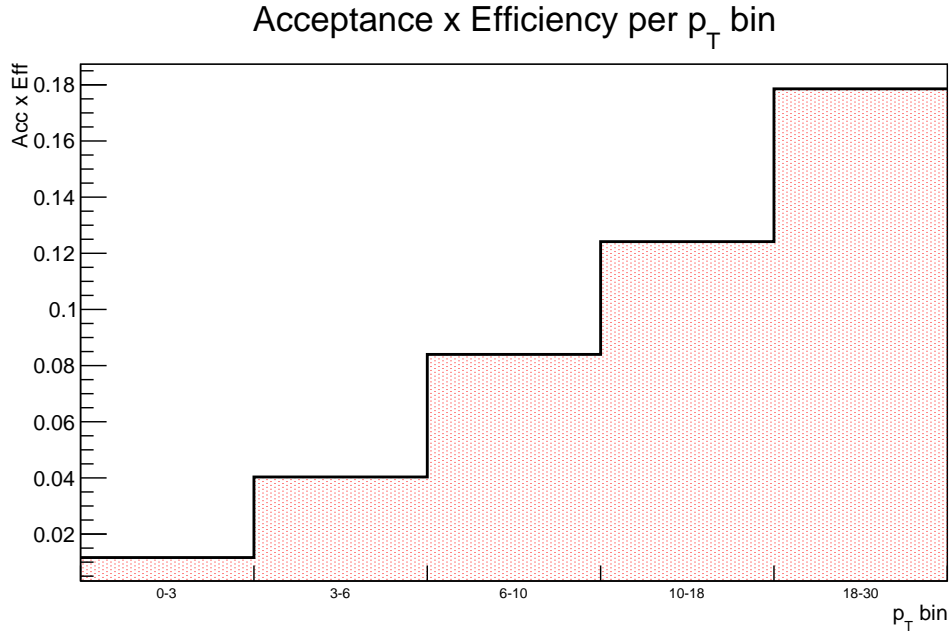


Figure 8.10: This histogram shows the acceptance times the efficiency per  $p_T$  bin for  $B^0$  detection and reconstruction in Monte Carlo pPb collisions at  $\sqrt{s_{NN}} = 5.02$  TeV.

### 8.3.2 Expectation in Data

#### Efficiency of reconstruction in Monte Carlo

Using the Monte Carlo data set LHC13d3.plus we have approximately 28.7 million events containing an enhanced number of  $B^0$ . In order to ignore the possible effects caused by forcing of specific decay channels we only look at the total number of  $B^0$  mesons that decay with the correct decay branch.

In total there are 9614  $B^0 \rightarrow \pi^+\pi^-\pi^-K^+$  created in the Monte Carlo data set. Of these there are 1867 of which all the final tracks are measured. So we find:

$$\text{Acc} = \frac{1867}{9614} = 19.42\%.$$

Next, we need to calculate the efficiency of the reconstruction. Of the 1867  $B^0 \rightarrow \pi^+\pi^-\pi^-K^+$  we manage to reconstruct 552  $B^0$  mesons using cuts. This results in the efficiency for the full  $p_T$  range:

$$\text{Eff} = \frac{552}{1867} = 29.6\%,$$

which gives us the factor for the full  $p_T$  range:

$$\text{Acc} \times \text{Eff} = 19.42\% \times 29.6\% = 5.74\%.$$

#### Number of $B^0$ mesons expected in measurement pPb 5.02 TeV data

Using these results we find the number of  $B^0 \rightarrow \pi^+\pi^-\pi^-K^+$  we expect to find in data per event:

$$N_{\text{Channel/event}} = N_{B^0/\text{event}} \times \mathbf{BR} \times \text{Acc} \times \text{Eff}.$$

We use the two literature values for beauty quark production from chapter 6.3 and the scale the result with the average number of binary collisions and the collision energy. The number of  $B^0$  mesons per event we find for the first and for the second value respectively are:

$$N_{\text{Channel/event}} = 2.46 \times 10^{-3} \times 7.27 \times 10^{-5} \times \frac{5.02}{7} \times 6.87 \times 5.74\% = \mathbf{50.58 \times 10^{-9}},$$

$$N_{\text{Channel/event}} = 3.57 \times 10^{-3} \times 7.27 \times 10^{-5} \times \frac{5.02}{7} \times 6.87 \times 5.74\% = \mathbf{73.4 \times 10^{-9}}.$$

If we instead assume an efficiency of 100% we get:

$$N_{\text{Channel/event}} = 2.46 \times 10^{-3} \times 7.27 \times 10^{-5} \times \frac{5.02}{7} \times 6.87 \times 19.42\% = \mathbf{171.1 \times 10^{-9}},$$

$$N_{\text{Channel/event}} = 3.57 \times 10^{-3} \times 7.27 \times 10^{-5} \times \frac{5.02}{7} \times 6.87 \times 19.42\% = \mathbf{248.3 \times 10^{-9}}.$$

This means that the total number of  $B^0$  mesons we can measure using this decay branch is approximately 248 per one billion events if we have a perfect efficiency. The acceptance is higher than in the pp Monte Carlo analysis while the efficiency is lower. This leaves more room for optimization of this analysis. Using the same calculation as above we show the expected number of  $B^0$  mesons per billion events per  $p_T$  bin in figure 8.11.

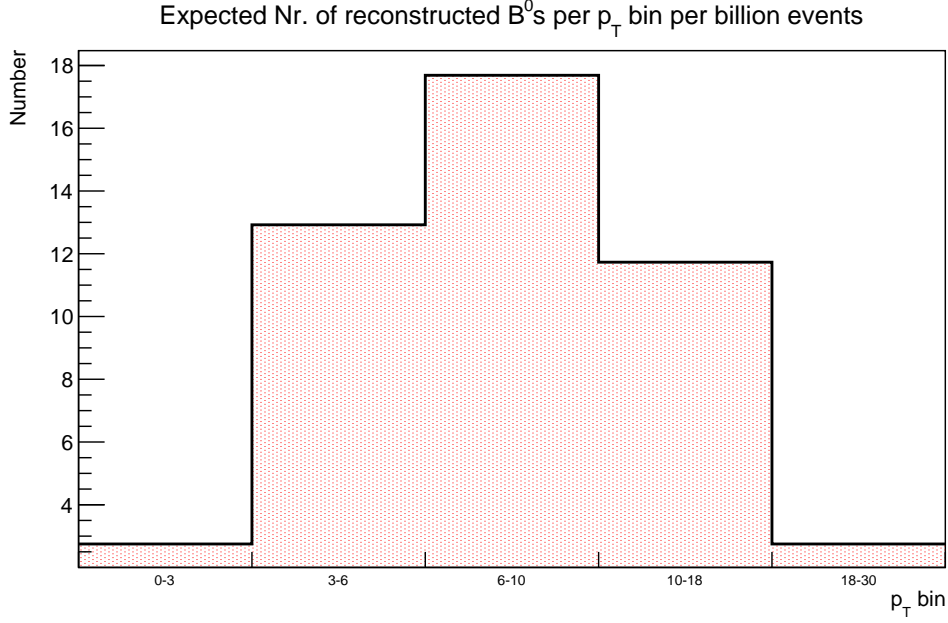


Figure 8.11: Using the reconstruction efficiency and the  $B^0$  production per  $p_T$  bin we get the average number of  $B^0$  we expect to find in one billion pPb collision events at  $\sqrt{s_{NN}} = 5.02$  TeV.

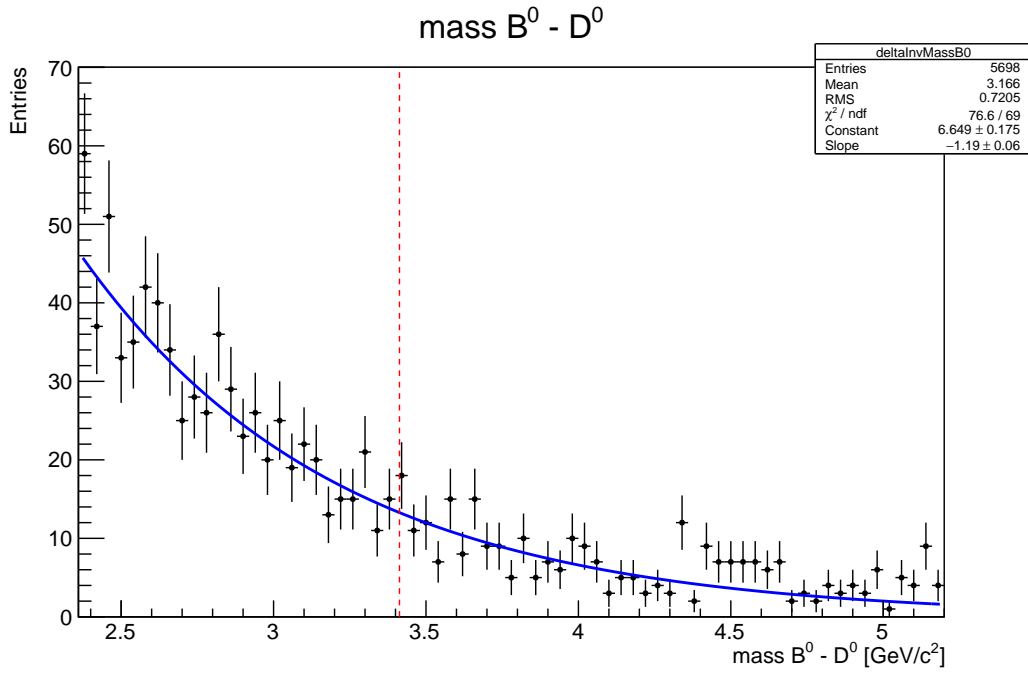


Figure 8.12: This graph shows the  $B^0 - D^0$  invariant mass result for the  $B^0$  candidates in real p-Pb collisions at  $\sqrt{s_{NN}} = 5.02$  TeV. The blue line shows an exponential fit of the background. The red dotted line show the PDG value for the  $B^0 - D^0$  mass.

### 8.3.3 Data

We use the data sets LHC13b and c. We have 93.6 million events, this means that we expect to measure:

$$N_{\text{Channel}} = N_{\text{Channel/event}} \times N_{\text{events}} = 50.58 \times 10^{-9} \times 93.6 \times 10^6 = 4.73$$

Where we use the conservative beauty production calculation. The  $p_T$  integrated results are shown in figure 8.12. We used the same cuts that were used for the Monte Carlo analysis. We cannot conclusively say to see a signal in this figure.

## 8.4 EMCal trigger exploration

We did a first test, using the pp  $\sqrt{s} = 7$  TeV data set LHC15a2a, to explore the effects of using an EMCal trigger. When we use an EMCal trigger we can trigger on the presence of a high energy electron. Since a significant number of  $B^0$  mesons decay semi-leptonically we could potentially increase the number of  $B^0$  mesons of the right channel per event by using an EMCal trigger.

We compare untriggered events with events that emit an electron with a momentum of at least one GeV/c in the direction of the EMCal ( $-0.7 < \eta < 0.7, 80^\circ < \phi < 187^\circ$ ). So we don't take detector effect and efficiency into account. Using these settings we find:

$$N_{\text{channel/event}}^{\text{triggered}} = 147/1.26 \times 10^6 = 1.17 \times 10^{-4}$$

$$N_{\text{channel/event}}^{\text{normal}} = 3034/28.2 \times 10^6 = 1.08 \times 10^{-4}$$

This means that with this trigger we would have 8.3% more  $B^0$  mesons per event. This is a small increase and this increase will probably become smaller when the full effects of using the EMCal are taken into account. A more detailed study will be required however to draw definite conclusions.

## Chapter 9

# Discussion and Conclusions

We have successfully developed an analysis framework for the ALICE experiment that reconstructs  $B^0$  mesons in both simulated and real data. The  $B^0$  mesons are fully hadronically reconstructed using the decay channel  $B^0 \rightarrow D^{*-}\pi^+ \rightarrow \bar{D}^0\pi^-\pi^+ \rightarrow \pi^-K^+\pi^-\pi^+$ . We have studied this decay in several types of collisions and calculated the expected number of detectable decays per event for these collisions in data.

The decay we have studied in this thesis has a small production cross section, so we need a large number of events to detect a signal. Roughly estimated, we will need a few billion pp events at  $\sqrt{s} = 7$  TeV or several hundred million p-Pb events at  $\sqrt{s_{NN}} = 5.02$  TeV at current efficiencies for first signs of the  $B^0 \rightarrow \pi^-K^+\pi^-\pi^+$  decay. ALICE has this number of events on tape, so a first signal might be observed if the analysis is successfully performed using these events.

Detection of the first signal is most likely in the full  $p_T$  integrated invariant mass spectrum and the  $3 < p_T$  invariant mass spectrum because the signal in these ranges has the highest significance. As the number of recorded events increases, it will become increasingly likely to see a signal in the central  $p_T$  bins ( $3 < p_T < 6$  [GeV/c],  $6 < p_T < 10$  [GeV/c],  $10 < p_T < 18$  [GeV/c]). Detection in the peripheral  $p_T$  bins ( $0 < p_T < 3$  [GeV/c],  $18 < p_T < 30$  [GeV/c]) will be harder due to a large background and a small signal respectively. The efficiency of cuts is very low at lower  $p_T$  values which makes a detection of a signal in the  $0 < p_T < 3$  [GeV/c] range unlikely, but we have not studied the optimal values for the  $p_T$  bin ranges so future studies might find a better range, which decreases the lower bound for detection.

The two most effective cuts are the cuts on the invariant mass of the reconstructed daughters and the pointing angles of the reconstructed particles. The ITS upgrade will result in a significant improvement of the pointing resolution which should contribute in cuts that remove more background and less signal. A Monte Carlo data set for the upgraded detector has been created for Pb-Pb collisions, so a future study on  $B^0$  mesons from Pb-Pb collisions can explore the effects of the upgrade.

The small cross section of the decay remains a challenge, but given enough statistics this analysis should be able to find a signal. If future studies result in higher efficiencies, we can expect to find a stronger signal or a signal in less collision events. We also identified several other decay channels with higher branching ratios than the decay channel used in the analysis in this thesis which are promising for future studies.

Using the analysis framework we have shown in Monte Carlo data that we can successfully reconstruct  $B^0$  mesons with the selected decay channel. We have also shown that we do not see a signal in current pp  $\sqrt{s} = 7$  TeV and p-Pb  $\sqrt{s_{NN}} = 5.02$  TeV data sets, and we have shown that this is conform expectations.



## Chapter 10

# Acknowledgment

The work I have done during the past year for this thesis has been very gratifying. Creating a new analysis framework is a lot of fun but there are also many steps that take a lot of time to do, and even more time to do well. Luckily, I had the constant support of my supervisors André Mischke and Alessandro Grelli, without their help I would not have been able to make this thesis.

The last year I also had the pleasure of working with all the people who work at the Institute of Subatomic Physics at Utrecht University. Many people have helped me with my work, and I want to thank especially my fellow master students Mike Sas, Daan Leermakers, and Luuk Vermunt for their help, friendship, and the many cups of coffee.

I am also grateful for all the people who have taught and helped me during my studies. It is only because of these people that I am where I am and have been able to study the beautiful complexity of the universe. Lastly, I want to thank my friends and family for all their help and love.

# References

- [1] J.H. Stiller, Full kinematic reconstruction of charged B mesons with the upgraded Inner Tracking System of the ALICE Experiment, Ph.D. thesis, Ruperto-Carola-University of Heidelberg, 2016.
- [2] V. Kucera, Study of strange particle production in jets with the ALICE experiment at the LHC, Ph.D. thesis, University of Strasbourg, 2016.
- [3] J. Wilkinson, Analysis of D0 and D+-meson production in pp and pPb collisions with ALICE at the LHC, Ph.D. thesis, Physikalisches Institut Universität Heidelberg, 2016.
- [4] D.A.M. Godoy, Elliptic azimuthal anisotropy of electrons from heavy-flavour decays in Pb-Pb collisions at 2.76 TeV measured with ALICE, Ph.D. thesis, University of Sao Paulo, 2013.
- [5] C. Jahnke, Measurement of electrons from heavy-flavour hadron decays in p-Pb at 5.02 TeV using TPC and EMCal detectors with ALICE at LHC, Ph.D. thesis, Ruprecht-Karls-Universität Heidelberg, 2016.
- [6] I. Sputowska, Correlations in Particle Production in Nuclear Collisions at LHC Energies, Ph.D. thesis, The Henryk Niewodniczanski Institute of Nuclear Physics - Polish Academy of Sciences, 2016.
- [7] A. Zimmermann, Production of strange hadrons in charged jets in PbPb collisions measured with ALICE at the LHC, Ph.D. thesis, Ruprecht-Karls-Universität Heidelberg, 2016.
- [8] A. Dainese, Charm production and in-medium QCD energy loss in nucleus-nucleus collisions with ALICE, Ph.D. thesis, Padova University, 2003.
- [9] ALICE collaboration, Centrality dependence of particle production in pPb collisions at  $\sqrt{s_{NN}} = 5.02$  TeV, arXiv:1412.6828v2, 2015.
- [10] R. Tieulent - ALICE collaboration, ALICE Upgrades: Plans and Potentials, arXiv:1512.02253v1, 2015.
- [11] J. van der Maarel, Azimuthal angular correlations of heavy flavour decay electrons and charged hadrons in proton-proton collisions at  $\sqrt{s} = 7$  TeV using the ALICE detector, Master Thesis, Utrecht University, 2013.
- [12] N. Mohammadi, Azimuthal angular correlations between heavy-flavour electrons and charged hadrons in semi-central lead-lead collisions at 2.76 TeV at ALICE, Master Thesis, Utrecht University, 2013.
- [13] A.M. Veen,  $D^{*+}$  reconstruction in proton-proton interactions at  $\sqrt{s} = 8$  TeV with the ALICE detector at the Large Hadron Collider, Master Thesis, Utrecht University, 2014.
- [14] M. Thomson, Modern Particle Physics, Cambridge University Press, 2013.
- [15] ALICE and CERN collaboration, <https://home.cern>, accessed December 2016.
- [16] Ta-Wei Wang for the CMS collaboration, B meson nuclear modification factor in Pb-Pb at 5.02 TeV with CMS, Hard Probes, 2016.

- [17] Kisoo Lee for the CMS collaboration, B production in pPb at 5.02 TeV from CMS, EDP Sciences, 2016.
- [18] Andrea Dubla for the ALICE collaboration, Measurements of heavy-flavour nuclear modification factor and elliptic flow in PbPb collisions at  $\sqrt{s_{NN}} = 2.76$  TeV with ALICE, Nuclear Physics A Volume 956, 2016.
- [19] <https://www.bnl.gov/newsroom/news.php?a=26716>, accessed January 2017.
- [20] Mangano, Nason, Ridolfi, Heavy-quark correlations in hadron collisions at next-to-leading order, Nucl. Phys. B 373 (1992) 295
- [21] L. Smirnova, Expected b-production at the LHC, <https://indico.cern.ch/event/94968/contributions/2124212/attachments/1107192/1579704/IHEPSmirnova2010.pdf>, accessed December 2016.
- [22] Particle Data Group, <http://www-pdg.lbl.gov/>, accessed December 2016.

